THE ASTROPHYSICAL JOURNAL, 335:40–56, 1988 December 1

EVIDENCE FOR A CENTRAL DARK MASS IN NGC 4594 (THE SOMBRERO GALAXY)

JOHN KORMENDY[1]
Dominion Astrophysical Observatory, Herzberg Institute of Astrophysics
Received 1988 February 29; accepted 1988 May 31

ABSTRACT

Stellar rotation velocities and velocity dispersions along the major and minor axes of NGC 4594 have been measured in effective seeing $\sigma_* = 0''.38$–$0''.47$ with the Canada-France-Hawaii Telescope. There is a clear kinematic signature of a nuclear disk of stars superposed on the bulge. Apart from its larger size, this is similar to the nucleus of M31. It rotates rapidly: the apparent rotation curve reaches an inner maximum of $V = 231 \pm 7$ km s^{-1} at $r = 5''.0$. The apparent velocity dispersion falls from $\sigma = 250 \pm 7$ km s^{-1} at the center to 181 ± 6 km s^{-1} at $r = 3''.7$. The latter is smaller than the local $\sigma \simeq 240$ km s^{-1} in the bulge. After subtraction of bulge light, the true outer dispersion of the nucleus is $\lesssim 100$ km s^{-1}. This and the shape of the isophotes show that the nucleus is a disk.

To search for a central black hole, three-dimensional velocity and velocity dispersion fields are found that fit the observations after projection and seeing convolution. The simplest good model has $V = 335$ km s^{-1} and $\sigma = 265r^{-0.5}$ km s^{-1} (100 km s$^{-1} \leq \sigma \leq 400$ km s^{-1}) at $r \leq 8''$. In all acceptable models, large velocities and velocity gradients imply that the total mass-to-light ratio rises by more than a factor of 10 at $r < 1''$ to values $M/L_V > 50$. This is much larger than normal for old stellar populations. Velocity anisotropies are not a major uncertainty because of the rapid rotation. Exploration of model parameter space shows that the central rise in M/L_V is a robust result independent of the assumed forms of $V(r)$ and $\sigma(r)$. Therefore the observations imply that NGC 4594 contains a central dark object, possibly a black hole, of mass $M_\bullet \sim 10^9\ M_\odot$.

Subject headings: galaxies: individual (NGC 4594) — galaxies: internal motions — galaxies: nuclei — galaxies: structure

I. INTRODUCTION

Stellar-kinematic evidence for dark central masses of 10^6–$10^8\ M_\odot$ has now been found in M32 (Tonry 1984, 1987; Dressler and Richstone 1988) and M31 (Dressler 1984; Kormendy 1987*a*, 1988*a*, *c*; Dressler and Richstone 1988). These are plausibly but not uniquely interpreted as supermassive black holes (BHs) like those postulated as engines for nuclear activity. Indirect evidence for a BH at the center of our Galaxy is provided by the observation that 2×10^{34} ergs s^{-1} of radio luminosity are emitted from a region as small as the orbit of Saturn around the Sun (Lo *et al.* 1985). The detection of BH candidates in all three Local Group galaxies with prominent bulge components (i.e., large central concentrations of stars) suggests that nuclear BHs may be common.

Black hole searches beyond the Local Group are more difficult, because sensitivity to $10^7\ M_\odot$ mass concentrations rapidly deteriorates with increasing distance (Richstone 1987, 1988). However, energy arguments suggest that BHs powering quasars can have masses $\gtrsim 10^9\ M_\odot$ (Rees 1984). Such objects can be detected as far away as the Virgo Cluster with the excellent resolution available at the Canada-France-Hawaii Telescope (CFHT) (Gaussian dispersion of a star profile $\simeq 0''.2$–$0''.4$). High-resolution photometry and spectroscopy are therefore being obtained for bright, early-type candidate galaxies, to study galaxy cores and to look for BHs (Kormendy 1985*a*, *b*, 1987*a*, *b*, 1988*a*, *b*; Kormendy 1988*c*, hereafter Paper I).

This paper discusses absorption-line spectroscopy of the prototypical Sa galaxy NGC 4594 (the Sombrero galaxy). NGC 4594 was chosen because it is as luminous as giant ellipticals ($M_B \simeq -22.7$ for an assumed distance of 18.0 Mpc) but nevertheless rotates rapidly enough so that velocity anisotropies are small (Kormendy and Illingworth 1982, hereafter KI; Jarvis and Freeman 1985). This simplifies the interpretation. Also, there is an inner peak in the stellar rotation curve at $\sim 5''$ (KI, although the published rotation curve was binned coarsely; Rubin *et al.* 1985; Jarvis 1987). The present data have two main implications. There is a rapidly rotating, "cold" nuclear disk of stars superposed on the bulge, and a central dark mass of $\sim 10^9\ M_\odot$.

II. OBSERVATIONS AND REDUCTION

The observation and data reduction procedures are described in Paper I. The measurements were made with the CFHT and Herzberg spectrograph (Salmon 1985). The detector was an RCA CCD ("RCA1": 316 × 498, 30 μm pixels; read noise $\sim 71e^{-1}$ pixel^{-1}; Walker *et al.* 1984). The spectrograph was used at f/4, giving a scale of $0''.435$ pixel^{-1}. The slit width was set at $0''.5$ to maximize spatial resolution without requiring excessive integration times. Measurements were made along the major and minor axes of NGC 4594, at position angles 90° and 0°, respectively. General parameters of the spectra are given in Table 1. The integration time and seeing σ_* are given for each spectrum in Table 2.

Special care was taken to estimate the spatial resolution as well as possible. The telescope was focused before every galaxy integration by taking a series of 10–20 s exposures of stars at various Cassegrain secondary-mirror positions. A final integration at the adopted focus was kept, and the full width at half of maximum intensity $\mathrm{FWHM}_{\mathrm{focus}}$ was measured. Since telescope flexure and guiding errors further degrade the resolution, a 180–300 s guided integration on a faint "seeing star" at the

[1] Visiting Astronomer, Canada-France-Hawaii Telescope, operated by the National Research Council of Canada, the Centre National de la Recherche Scientifique of France, and the University of Hawaii.

TABLE 1
PARAMETERS OF SPECTRA

Parameter	Value
Slit length	2'.0
Scale along slit	0".44 pixel^{-1}
Slit width	0".5
Wavelength range (over 512 pixels)	5064–5684 Å
Reciprocal dispersion	1.22 Å pixel^{-1}
Reciprocal dispersion	68 km s^{-1} pixel^{-1}
Comparison line FWHM	2.0 pixel
Instrumental velocity dispersion	57 km s^{-1}
Standard star	η Cyg
Standard star spectral type	K0 III

NOTE.—The resolution of the spectrograph is determined mainly by the camera.

mean hour angle of the observations was obtained immediately after each galaxy exposure. The ratio of FWHM values for seeing and focus stars measured at the same zenith distance is $\mathrm{FWHM_{seeing}}/\mathrm{FWHM_{focus}} = 1.06 \pm 0.03$, as in Paper I. That is, guiding errors do not greatly affect the resolution. Guiding may be sligtly worse for galaxy images, but, as in M31, the nucleus of NGC 4594 is small and bright. Values of $\sigma_* = \mathrm{FWHM_{seeing}}/2.35$ are given for each integration in Table 2. The seeing was better than this. Guide stars almost disappeared in the 0".5 wide slit, so the seeing contribution to σ_* was $\lesssim$0".25. The spatial resolution is limited by the spectrograph. However, good seeing is important, because it determines the origin in the galaxy of the light that passes through the slit. No single parameter completely characterizes the resolution; in the rest of the discussion I will use σ_* as defined above.

Differential refraction was small. The largest mean zenith distance was 36° (1^h10^m E hour angle for the 2700 s integration on the major axis). Here differential refraction between 5374 Å and the effective wavelength $\sim$5000 Å of the acquisition TV (S-20 photocathode observing at $B-V=1$) was $\sim$0".08.

Instrumental reduction of RCA CCD data is routine (Paper I). Geometric distortion corrections were calculated using the "longslit" package in the National Optical Astronomy Observatories Image Reduction and Analysis Facility (IRAF) (Tody *et al.* 1986). The spectra were then rewritten without distortion on a ln λ scale for the Fourier program.

Spectra of MK standard stars chosen from Morgan and Keenan (1973) were observed and reduced similarly. Since their images can be smaller than the slit, stars were trailed along the slit at position angles slightly different from 0° or 90°. After rectification, intensities were averaged along the slit to produce one-dimensional spectra with the proper instrumental dispersion. In the Fourier analysis, different K0–K2 III stars gave almost identical results; the adopted star (Table 1) is essentially arbitrary.

Velocities V and velocity dispersions σ were calculated using a Fourier quotient program (Sargent *et al.* 1977; Schechter and Gunn 1979) originally imported to the Dominion Astrophysical Observatory from Kitt Peak National Observatory. All galaxy spectral lines were used. The final velocities and dispersions are listed in Table 2. The adopted center is at the row of brightest pixels along the slit. Each major-axis spectrum was reduced as observed and after subtraction of the bulge (§ III*d*); the adopted center and systemic velocity are the same for both reductions.

Because a wide range of velocity dispersions is present in NGC 4594, it is unusually important to make a careful choice of the smallest frequency $k_{\min}$ used in the Fourier fit. To measure large velocity dispersions, I need to use as small a value of $k_{\min}$ as possible. But at low frequencies the Fourier quotient is affected by imperfect continuum subtraction. After considerable experimentation, I chose $k_{\min} = 1/f$, where $f = 0.1$ is the fraction of the spectra that was masked at each end (see Brault and White 1971, p. 180; this was also the value used in Paper I). The velocity dispersion scale was verified by comparing measurements of other galaxies observed during the run with published results (Whitmore, McElroy, and Tonry 1985). Problems with the wavenumber range used in the Fourier fit are discussed further in § V*a*.

Only one external check of the NGC 4594 results is possible. The central dispersion is $\sigma_0 = 250 \pm 7$ km s^{-1}; Whitmore, McElroy, and Tonry (1985) found a mean $\sigma_0 = 256 \pm 8$ km s^{-1} from three different authors. The major-axis rotation velocities are larger at all radii than in KI. This is expected from the nearly edge-on inclination, the bad seeing of the major-axis KI observations ($\sigma_* = 2".1$ compared with 0".38–0".41 here), and the presence of a rapidly rotating nuclear disk (§ III). For similar reasons the present rotation velocities are also higher than those observed by Rubin *et al.* (1985) and by Jarvis (1987).

More disturbing is the observation of 88 ± 8 km s^{-1} of rotation in two minor-axis spectra taken on different nights. This could result from incorrect centering of the slit by an amount comparable to the radius $r \simeq 0".5$ at which the major-axis rotation curve reaches 88 km s^{-1}. It is not easy to see how this could have happened. Differential refraction has the correct sign, but at 0^h35^m W hour angle, the slit would have been set too far east by only 0".02. Another possibility is that the rotation curve is symmetric about a point different from the brightest pixel (cf. M31). However, any asymmetry is $\lesssim$0".05. Or the photometric center at $r \sim 2"$, which has heavy weight in the guiding, could be different from the brightest point. A V-band image taken at the Cassegrain focus (scale = 0".215 pixel^{-1}) suggests the presence of a small asymmetry of the required sign, but the magnitude is only $\sim$0".06. None of these effects is clearly large enough to account for the observations. On the other hand, even if nonzero velocities along the minor axis are due to guiding errors, they are unlikely to affect the conclusions of this paper. The minor-axis dispersion measurements still refer adequately to the bulge. For the major-axis spectra, any guiding errors perpendicular to the slit decrease the kinematic gradients; then the central masses that I derive are lower limits. However, guiding is easiest when the major axis is aligned with the slit.

III. KINEMATICS AND PHOTOMETRY: EVIDENCE FOR A NUCLEAR DISK

a) Kinematics from Composite Spectra of Bulge and Nucleus

The rotation and dispersion profiles are illustrated in Figure 1. The apparent rotation curve rises rapidly to an inner maximum of 231 ± 7 km s^{-1} at $r = 5".0$ (all quoted errors are internal errors). Most of the rise in $V(r)$ occurs in the central 1".5 and is unresolved. Meanwhile, the apparent velocity dispersion falls from 250 ± 7 km s^{-1} at the center to 181 ± 6 km s^{-1} at $r = 3".7$. The latter is certainly smaller than the dispersion in the bulge, 240 ± 4 km s^{-1} at $r \lesssim 5"$ along the minor axis. At $r > 5"$ along the major axis, the rapidly rotating component contributes less and less light: $V(r)$ fall and $\sigma(r)$ rises to the rotation and dispersion curves of the bulge. For example, at $r \simeq 10"$, $\sigma \sim 240$ km s^{-1}, equal to the bulge dispersion.

TABLE 2

ROTATION AND VELOCITY DISPERSION DATA

NGC 4594 Major Axis
Exp. = 2700 s P.A. = 90° σ_* = 0.″41

r	V	$\epsilon(V)$	σ	$\epsilon(\sigma)$
−24.8	−219	22	184	26
−18.4	−176	26	177	32
−13.5	−181	25	206	30
−9.3	−177	30	261	34
−7.5	−176	21	230	25
−6.0	−206	17	233	20
−5.2	−233	20	207	23
−4.8	−245	15	170	19
−4.3	−218	19	203	22
−3.9	−205	17	185	20
−3.5	−226	13	160	16
−2.8	−215	9	180	10
−1.9	−187	7	186	9
−1.3	−171	11	202	12
−0.9	−128	10	223	12
−0.4	−65	11	247	13
0.0	3	12	260	14
0.4	88	12	246	13
0.9	127	11	222	13
1.3	153	11	201	13
2.0	175	8	208	10
2.8	197	9	202	11
3.5	211	14	182	16
3.9	216	14	172	17
4.3	224	17	213	20
4.8	219	18	189	22
5.2	245	20	198	24
6.4	220	15	197	17
8.6	189	22	242	25
10.8	163	28	229	32
14.0	171	24	207	29
23.2	233	22	194	26
33.8	286	15	115	19

NGC 4594 Major Axis −Bulge = C
Exp. = 2700 s P.A. = 90° σ_* = 0.″41

r	V	$\epsilon(V)$	σ	$\epsilon(\sigma)$
−7.7	−315	17	97	24
−6.3	−298	20	136	24
−5.7	−296	20	125	26
−5.2	−284	17	149	21
−4.8	−285	14	127	18
−4.3	−276	16	137	20
−3.9	−250	16	144	20
−3.5	−257	12	121	15
−3.0	−246	11	139	14
−2.6	−248	10	145	13
−2.2	−214	10	157	12
−1.7	−204	9	165	11
−1.3	−190	10	180	12
−0.9	−141	10	213	12
−0.4	−71	12	245	13
0.0	6	13	262	14
0.4	101	12	243	14
0.9	144	11	210	14
1.3	176	10	184	13
1.7	195	11	183	14
2.2	219	11	184	14
2.6	233	12	176	15
3.0	243	13	159	16
3.5	257	12	134	16
3.9	266	12	119	16
4.3	280	17	160	21
4.8	284	16	128	20
5.2	314	17	124	21
5.9	315	17	106	22
6.9	307	17	111	21

NGC 4594 Major Axis −Bulge = N
Exp. = 2700 s P.A. = 90° σ_* = 0.″41

r	V	$\epsilon(V)$	σ	$\epsilon(\sigma)$
−29.2	−324	17	77	27
−7.8	−314	19	99	25
−6.3	−307	19	133	24
−5.7	−307	19	113	25
−5.2	−296	17	142	21
−4.8	−296	14	118	18
−4.3	−293	16	122	20
−3.9	−271	15	131	19
−3.5	−271	11	110	15
−3.0	−264	11	122	13
−2.6	−266	10	128	13
−2.2	−234	10	139	12
−1.7	−222	9	149	11
−1.3	−210	10	166	12
−0.9	−160	10	201	12
−0.4	−84	12	239	14
0.0	3	14	263	15
0.4	110	13	240	16
0.9	160	12	201	15
1.3	192	10	168	12
1.7	215	11	161	13
2.2	239	11	163	13
2.6	253	11	153	14
3.0	260	13	142	16
3.5	271	12	118	15
3.9	279	12	102	17
4.3	296	16	139	19
4.8	297	15	109	19
5.2	323	16	111	21
5.9	322	17	99	22
6.9	308	18	108	24
8.6	319	17	112	22
12.2	312	21	119	28
23.0	340	22	118	28
33.7	313	12	79	16

NGC 4594 Major Axis
Exp. = 1800 s P.A. = 90° σ_* = 0.″38

r	V	$\epsilon(V)$	σ	$\epsilon(\sigma)$
−23.0	−250	24	167	31
−12.8	−160	21	191	24
−7.9	−191	20	201	24
−5.3	−219	13	178	15
−3.4	−209	11	189	12
−2.2	−187	8	189	9
−1.1	−156	9	210	10
−0.4	−94	13	238	15
0.0	−10	14	246	16
0.4	64	13	247	15
1.1	142	9	223	11
2.1	192	8	191	10
3.2	206	13	181	15
4.1	212	15	194	17
5.0	243	19	220	22
5.9	213	20	190	24
7.8	215	16	220	18
11.3	180	27	219	31
15.4	170	26	189	32
32.7	300	19	177	23

NGC 4594 Major Axis −Bulge = C
Exp. = 1800 s P.A. = 90° σ_* = 0.″38

r	V	$\epsilon(V)$	σ	$\epsilon(\sigma)$
−5.6	−285	12	105	16
−4.1	−272	13	140	16
−3.3	−240	12	155	15
−2.4	−229	9	160	11
0.0	−15	14	246	16
±0.4	90	10	236	11
±0.9	149	10	213	11
±1.3	186	9	189	10
±1.7	191	9	166	11
2.4	232	11	164	13
3.2	240	12	146	15
4.3	267	13	158	16
5.7	293	16	122	20
7.5	311	11	89	15

NGC 4594 Major Axis −Bulge = N
Exp. = 1800 s P.A. = 90° σ_* = 0.″38

r	V	$\epsilon(V)$	σ	$\epsilon(\sigma)$
−5.1	−298	14	90	19
−4.1	−283	12	121	16
−3.3	−256	11	140	14
−2.4	−244	9	142	11
0.0	−18	16	242	18
±0.4	83	10	226	12
±0.9	146	9	198	11
±1.3	182	9	168	10
±1.7	216	13	144	12
2.4	255	10	139	12
3.2	264	12	122	15
4.3	291	13	132	16
5.6	311	15	109	21
7.6	331	13	86	19
14.9	318	21	103	28
36.1	357	18	117	23

TABLE 2—*Continued*

NGC 4594 Minor Axis

Exp. = 4500 s P.A. = 0° σ_* = 0.″47

r	V	$\epsilon(V)$	σ	$\epsilon(\sigma)$
−6.8	−13	20	183	25
−3.9	4	23	251	26
−1.3	36	9	235	10
−0.4	80	8	231	10
0.0	88	8	246	10
0.4	77	9	239	11
1.1	43	9	245	10
2.4	1	15	244	16
5.0	−2	17	227	20
8.2	13	22	217	26

Beyond 10″ radius the main disk of the galaxy becomes important; then $V(r)$ rises and $\sigma(r)$ falls to values characteristic of disks (KI).

The small velocity disersion at $r \simeq 4''$ and the rapid rotation imply that there is a distinct nuclear disk superposed on the bulge. This is kinematically similar to the nucleus of M31 (Paper I), but more extreme. In M31 the fact that the outer nuclear dispersion is smaller than that of the bulge is apparent only after subtraction of bulge light. The conclusion that the nucleus of M31 is a disk is uncertain, because the apparent axial ratio of 0.6–0.75 is consistent with a disk seen 13° from edge-on only if the nucleus is barlike and seen nearly end-on. In NGC 4594 there is no doubt, because the galaxy is essentially edge-on and because the isophotes of the nucleus are highly flattened.

b) Brightness Distribution

The nuclear disk is visible in the brightness distribution. Two images are available. The first is a 10 m RCA1 CCD image in V, obtained at the Cassegrain focus (scale = 0.″215 pixel^{-1}). The seeing was poor, $\sigma_* \simeq 0.''58$. Fortunately, J. B. Hutchings kindly obtained an image with $\sigma_* = 0.''35$ in 1988 January, after most of the analysis of this paper was completed. This is a 100 s V exposure with the "RCA2" CCD at prime focus; the scale is 0.″206 (15 μm pixel)$^{-1}$. Major- and minor-axis cuts through the brightness distribution are given for both images in Table 3. The central isophotes in the better image are shown in Figure 2 and their axial ratios are shown in Figure 3.

Between ~3″ and ~8″ radius along the major axis the isophotes show cuspy extensions characteristic of edge-on disks. These were still more pronounced on the guiding TV during the spectroscopic observations, when the seeing $\sigma_* \lesssim 0.''25$ was better than during the photometry. Figure 3 shows that the isophotes appear flattest between 3″ and 5″ radius; they are flatter than they seem near the center also, but seeing forces

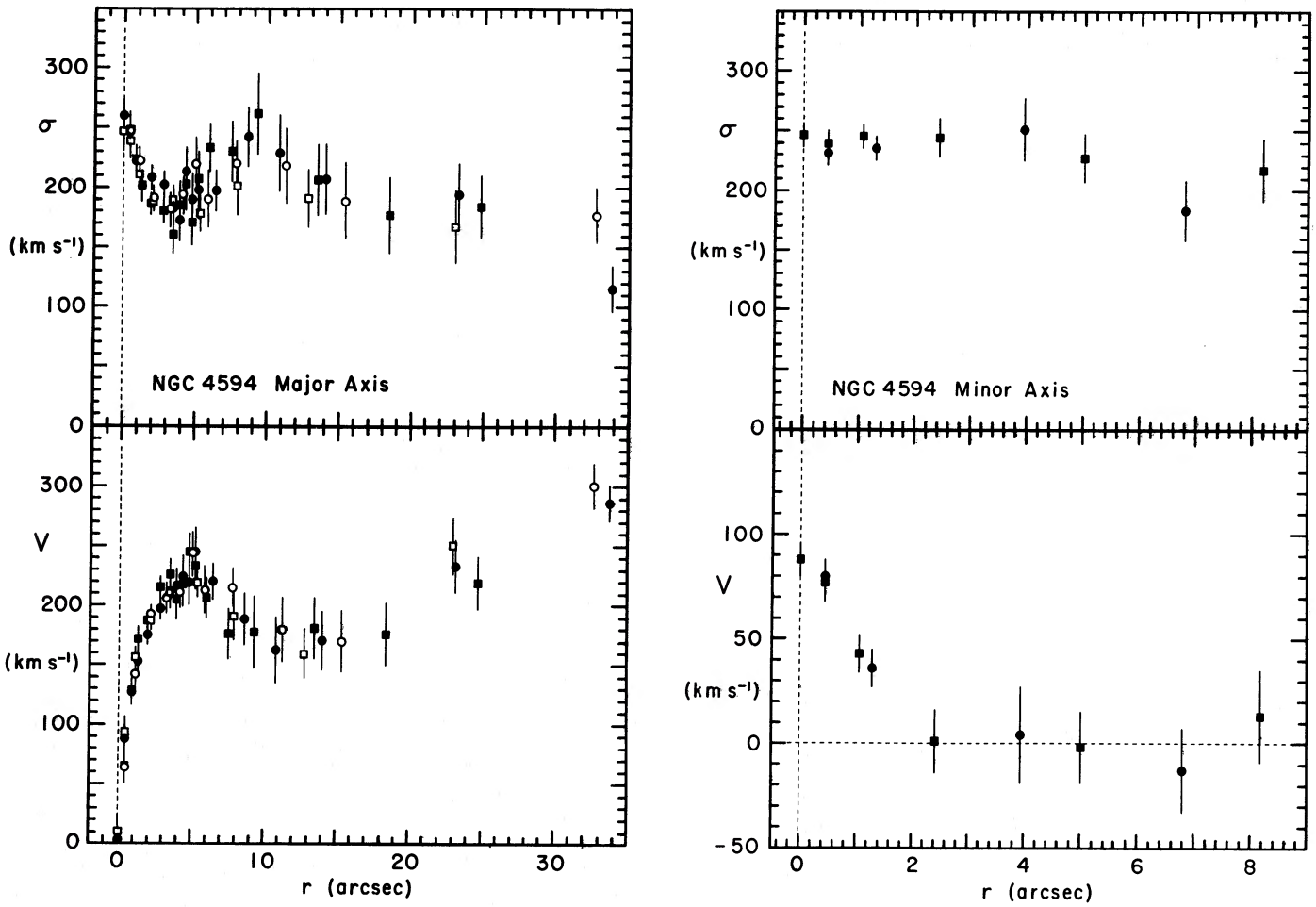

FIG. 1.—Folded rotation and dispersion profiles along the major and minor axes of NGC 4594. Central points are separated by 0.″44. Circles and squares refer to opposite sides of the center. In the left-hand panels, the closed symbols are for the 2700 s integration and the open symbols for the 1800 s integration.

TABLE 3

A. BRIGHTNESS PROFILE OF NGC 4594: FIRST IMAGE

r	μ_V	r	μ_V
Major Axis			
−1.97.....	15.52	6.13.....	16.62
−1.75.....	15.44	6.56.....	16.71
−1.54.....	15.38	6.99.....	16.80
−1.32.....	15.31	7.42.....	16.89
−1.11.....	15.23	7.85.....	16.97
−0.89.....	15.16	8.28.....	17.05
−0.68.....	15.09	8.71.....	17.12
−0.46.....	15.02	9.25.....	17.20
−0.25.....	14.97	9.90.....	17.28
−0.03.....	14.95	10.54.....	17.36
0.18.....	14.96	11.19.....	17.44
0.40.....	15.00	11.83.....	17.51
0.61.....	15.05	12.68.....	17.59
0.83.....	15.13	13.77.....	17.67
1.04.....	15.20	14.83.....	17.77
1.26.....	15.27	15.92.....	17.85
1.47.....	15.34	16.98.....	17.91
1.69.....	15.41	18.07.....	17.95
1.90.....	15.49	19.14.....	17.99
2.15.....	15.56	20.21.....	18.04
2.36.....	15.63	21.28.....	18.08
2.58.....	15.69	22.36.....	18.11
2.80.....	15.76	23.40.....	18.14
3.01.....	15.82	24.69.....	18.16
3.23.....	15.88	26.20.....	18.20
3.44.....	15.94	27.70.....	18.21
3.66.....	16.00	29.21.....	18.23
3.87.....	16.07	30.93.....	18.26
4.09.....	16.12	32.86.....	18.28
4.30.....	16.18	34.80.....	18.32
4.51.....	16.24	36.73.....	18.37
4.73.....	16.30	38.67.....	18.41
4.94.....	16.35	40.60.....	18.44
5.27.....	16.42	42.54.....	18.49
5.70.....	16.52	44.47.....	18.55
Minor Axis (North Side)			
0.01.....	14.95	5.71.....	17.31
0.23.....	14.99	6.14.....	17.39
0.44.....	15.08	6.57.....	17.48
0.66.....	15.22	7.00.....	17.54
0.87.....	15.39	7.43.....	17.61
1.09.....	15.56	7.85.....	17.67
1.30.....	15.72	8.29.....	17.73
1.52.....	15.87	8.72.....	17.78
1.73.....	16.02	9.26.....	17.86
1.95.....	16.15	9.90.....	17.94
2.16.....	16.26	10.55.....	18.01
2.38.....	16.36	11.19.....	18.09
2.59.....	16.46	11.84.....	18.17
2.81.....	16.55	12.70.....	18.24
3.02.....	16.63	13.77.....	18.32
3.24.....	16.70	14.85.....	18.43
3.45.....	16.77	15.92.....	18.52
3.67.....	16.84	17.00.....	18.61
3.88.....	16.90	18.07.....	18.71
4.10.....	16.95	19.15.....	18.79
4.31.....	17.01	20.22.....	18.88
4.53.....	17.07	21.30.....	18.97
4.74.....	17.11	22.37.....	19.04
4.96.....	17.16	23.44.....	19.13
5.28.....	17.23	24.52.....	19.18

NOTE.—Radii r are in arcseconds. Along the major axis, $r < 0$ on the west side; at $|r| > 2''$, data on both sides of the center are averaged. The V-magnitude zero point is from Burkhead 1986 and Jarvis and Freeman 1985. The seeing was $\sigma_* = 0''.58$.

TABLE 3—*Continued*

B. BRIGHTNESS PROFILE OF NGC 4594: SECOND IMAGE

r	μ_V	r	μ_V
Major Axis			
−1.06.....	15.20	1.85.....	15.47
−0.85.....	15.13	2.06.....	15.53
−0.65.....	15.03	2.37.....	15.63
−0.44.....	14.94	2.78.....	15.75
−0.23.....	14.87	3.19.....	15.86
−0.03.....	14.84	3.61.....	15.98
0.18.....	14.86	4.12.....	16.14
0.38.....	14.93	4.74.....	16.30
0.59.....	15.01	5.46.....	16.47
0.79.....	15.11	6.28.....	16.66
1.00.....	15.20	7.11.....	16.84
1.24.....	15.27	7.93.....	17.01
1.44.....	15.34	8.75.....	17.14
1.65.....	15.40	9.68.....	17.28
Minor Axis (North Side)			
0.10.....	14.78	2.06.....	16.20
0.31.....	14.89	2.47.....	16.40
0.52.....	15.06	2.88.....	16.56
0.72.....	15.25	3.30.....	16.69
0.93.....	15.43	3.61.....	16.79
1.13.....	15.60	3.81.....	16.85
1.34.....	15.78	4.22.....	16.98
1.55.....	15.91	4.84.....	17.12
1.75.....	16.03	5.91.....	17.35

NOTE.—Along the major axis, data on both sides of the center at $|r| > 1''$ are averaged. The seeing was $\sigma_* = 0''.35$.

b/a to approach unity as r goes to zero. At larger radii the isophotes are roundest at 10″–15″ radius; here the nucleus has faded into the bulge. Still farther out, the isophotes becoming flatter again because of the main disk. All this is consistent with the spectroscopic results.

Similar conclusions were reached by Burkhead (1986) in a careful photometric study of NGC 4594. He already concluded that there is an inner disk, and that this "appears quite thin, being only one-tenth the width of the [main] disk. ... The brightness of the inner disk ... rises to a maximum at 5 arcsec and declines to a minimum at 11–12 arcsec, where the [main] disk begins" (see his Fig. 11). At $r \sim 12''$ the axial ratio (Fig. 3 here) does not reach the value he finds for the bulge. This may indicate that the two disks still contribute some light. However, it is clear from the kinematics and from Figure 4 below that the contribution is small. Burkhead goes on to evaluate the disk surface brightness: he stretches the minor-axis profile by the major-to-minor axis ratio a/b of the bulge and then subtracts the result from the major-axis profile. From this he concludes that the nuclear disk "does not appear to continue to the [center] but ends at $a \sim 3$ arcsec." However, his procedure guarantees this conclusion even if the nucleus contributes all of the light at the center, because the central pixel is common to both axes. The rapid rotation shows that the nuclear disk continues to the center.

Figure 4 shows major- and minor-axis composite profiles $\mu(r)$ constructed from the present data and from published photometry. The magnitude zero point is from Burkhead (1986) and from Jarvis and Freeman (1985). The other profiles are shifted in μ to minimize the scatter; the shifts are determined to $\lesssim 0.02$ mag arcsec^{-2}. Near the center the profiles are

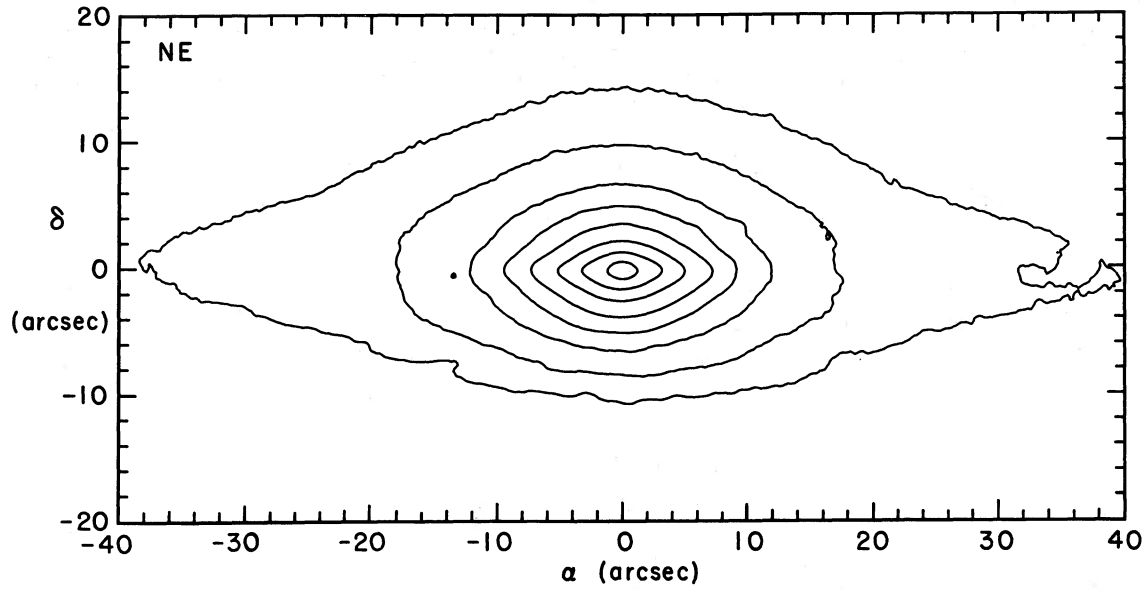

FIG. 2.—Central isophotes of NGC 4594, from a 100 s, V-band CCD exposure (scale 0".206 pixel^{-1}). North is up and east is to the left. The image has been smoothed with a Gaussian of radius 1 pixel; the effective resolution is $\sigma_* = 0".41$.

affected by seeing and in some cases by photographic saturation. At large radii, the spectra are not perfectly flat-fielded. However, the scatter over most of each profile is remarkably small, only a few hundredths of a mag arcsec^{-2}. In particular, brightnesses along the spectrograph slit agree well with the imaging results.

Inner parts of star profiles are shown in Figure 4 for the data with the best spatial resolution. These give an apparent central surface brightness of 14.83 ± 0.02 mag arcsec^{-2}. When corrected for Galactic absorption and for the mean seeing $\sigma_* \simeq 0".42$, the central surface brightness is $\mu_0 \simeq 14.39$ V mag arcsec^{-2}, and the half-brightness core radius is $r_c \simeq 1".22$. In bulges and elliptical galaxies, r_c and μ_0 correlate with absolute magnitude M_B; more luminous galaxies have larger cores of lower central surface brightness. But the nucleus of NGC 4594 is 2.0 mag arcsec^{-2} brighter and a factor of 3.4 smaller than normal for a bulge of $M_B = -21.9$ (NGC 4594 is the brightest-M_B open circle in Fig. 2 of Kormendy 1987*b*). This

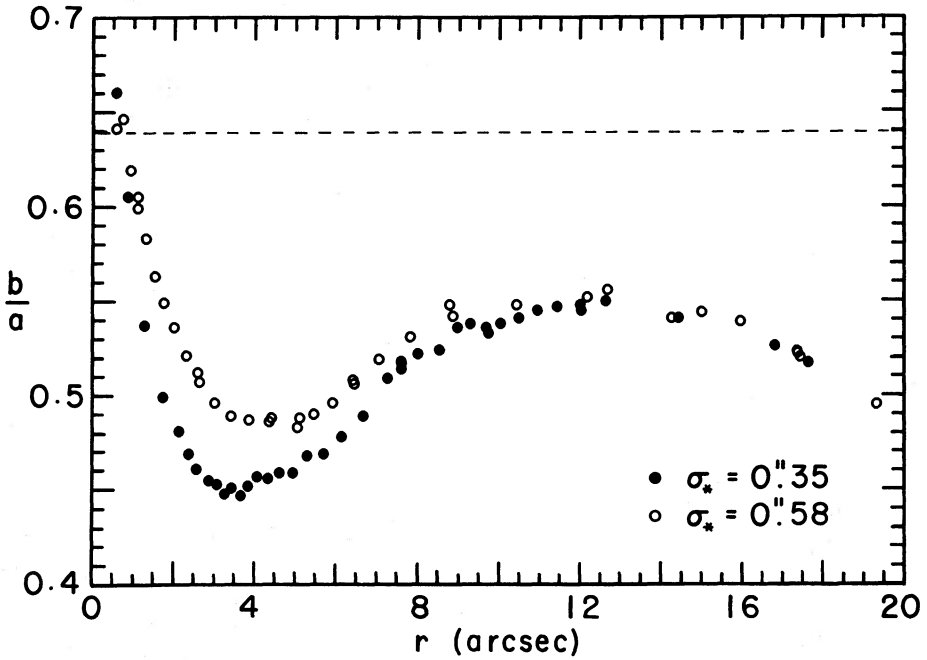

FIG. 3.—Isophote axial ratio as a function of major-axis radius near the center of NGC 4594. Note that b/a is the ratio of the shortest to the longest radius of an isophote and not the axial ratio of a fitted ellipse. The filled circles are from the unsmoothed version of the image shown in Fig. 2, the open circles from the poor-seeing RCA1 image. The dashed line in Burkhead's (1986) estimate of the shape of the bulge, i.e., the mean axial ratio $b/a = 0.639$ found by excluding the region near the major axis that is dominated by the disk. The apparent axial ratio goes to unity at the center because of seeing.

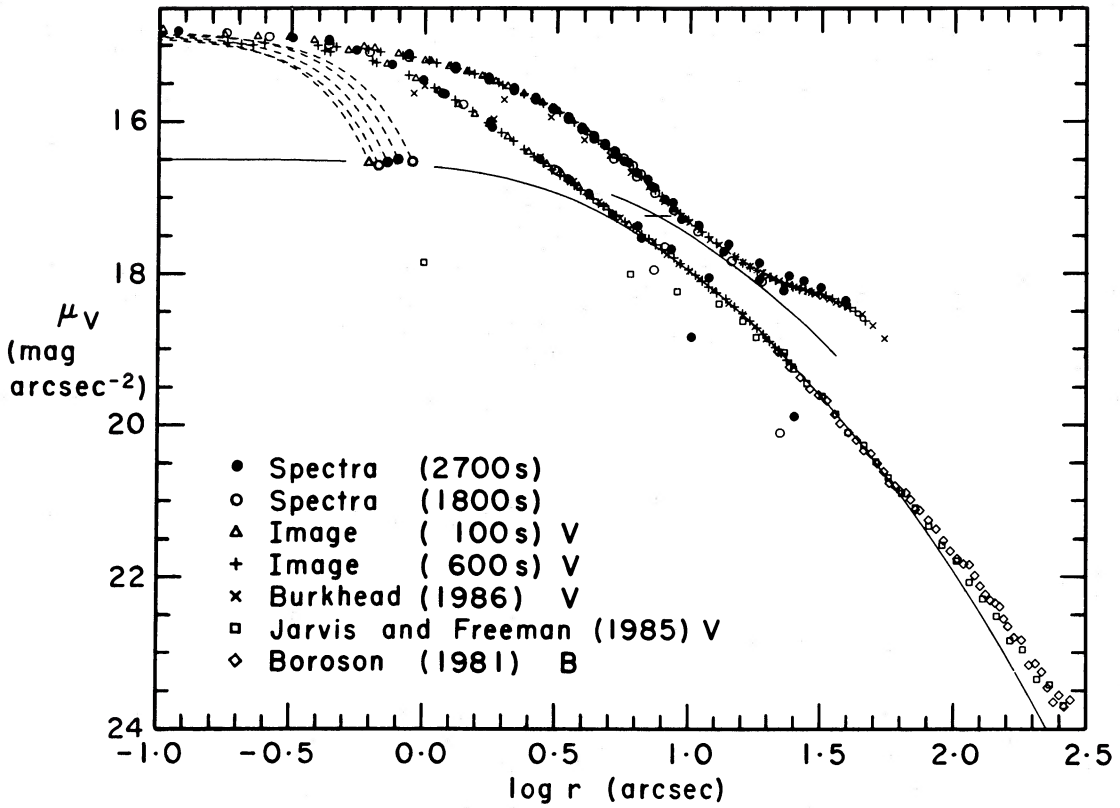

FIG. 4.—Composite major- and minor-axis brightness profiles in NGC 4594. Sources of the photometry are given in the key. The dashed lines are star profiles for the best-resolution data, i.e., the 100 s V image ($\sigma_* = 0''.35$) and the spectra ($\sigma_* = 0''.38$–$0''.47$; see Table 2). The curve is a fit of the average nonisothermal core profile of elliptical galaxies to the minor-axis data. The arc shows this scaled to the major axis by $\log(a/b) = 0.195$; it is plotted out to the maximum radius of the kinematic measurements. The horizontal tick on the arc shows the surface brightness 17.23 V mag arcsec^{-2} at $10''$. The extra light above these fits is attributed to the nuclear disk.

again is due to the extra nuclear disk, just as a similar deviation for M31 (faintest-M_B open circle in the same figure) is due to its nucleus.

c) *Nuclear Disk Luminosity Models*

I will use two different estimates of the relative brightness contributions of the bulge and nuclear disk. Most of the analysis is based on a conservative bulge subtraction. Photometry and kinematics both imply that the bulge contributes essentially all of the light at $r \simeq 10''$. Here $\mu = 17.23$ V mag arcsec^{-2}; I assume that this is the bulge brightness underlying the spectra at $r \leq 10''$. Figure 5 (*upper panel*) shows the major-axis profile after this is subtracted. Also shown are two luminosity models used in the analysis. Model "C" (for cutoff) has unprojected brightness

$$I(r) \propto e^{-r/r_0}\left(1 + \frac{r_\bullet}{r}\right)^{7/4} C(r)\,, \qquad (1)$$

where $C(r) = 1$ at $r \leq r_1$, $[(10 - r)/(10 - r_1)]^2$ at $r_1 < r < 10''$, and zero at $r \geq 10''$. This model is basically an exponetial of scale length r_0; it is modified to go to zero intensity at $r = 10''$, and sufficient extra light is included at the center to give an essentially perfect fit. For the extra light I use the functional form predicted by Bahcall and Wolf (1976) for the cusp around a black hole. In principle,

$$r_\bullet = GM_\bullet/\sigma_{00}^2\,, \qquad (2)$$

where $M_\bullet$ is the mass of the black hole and σ_{00} is the unperturbed central velocity dispersion. However, σ_{00} is never known. Therefore r_0, $r_\bullet$, and r_1 are to be regarded only as parameters found by fitting the projected and seeing convolved profile to the photometry with $\sigma_* = 0''.40$ (spectra) and $\sigma_* = 0''.58$ (image). This gives $r_0 = 2''.29$, $r_\bullet = 0''.26$, and $r_1 = 8''.3$. The image with $\sigma_* = 0''.35$ confirms that these parameters are a good fit to the brightness distribution. The results are insensitive to r_1 and to the form of the outer brightness cutoff.

I will also need an alternative nuclear disk model "N," which is an attempt to replace the black hole cusp factor $(1 + r_\bullet/r)^{7/4}$ by a stellar nucleus added to the exponential. The nucleus has magnitude $V = 16.3$; the best-fitting exponential has $r_0 = 2''.08$ and $r_1 = 8''.8$. Their sum is too cuspy to be a good fit to the photometry (Fig. 5), but it provides a useful "error bar" in § V.

To explore the sensitivity of the results to the bulge subtraction, a second and more complicated procedure is used for some models. This is also used in Kormendy and Westpfahl (1989), where accurate bulge subtraction at $r \gtrsim 10''$ is required.

In general, bulges and ellipticals have core profiles similar to projected isothermal spheres, with departures (too much light at the center) that correlate very roughly with luminosity (Lauer 1985; Kormendy 1985*a*). Almost all ellipticals that are well resolved with the CFHT have the same slightly nonisothermal profile (Kormendy 1985*a*, Fig. 1). This mean profile has been fitted to the inner "shoulder" in the minor-axis

profile in Figure 4. The profile of NGC 4594 is slightly shallower than this at large radii, like other bulges that are a little less isothermal than ellipticals (Kormendy 1985*a*, Fig. 2). If this is also true near the center, then the illustrated fit underestimates the bulge brightness underlying the nucleus. Therefore, this fit to the minor axis, and the same fit stretched along the major axis by $a/b = 1/0.639$ (Burkhead 1986) are still a conservative estimate of the bulge profile near the center.

Of course, this fit is uncertain. The bulge and nuclear brightness profiles are much less well distinguished in NGC 4594 than in M31. However, several consistency checks suggest that the fit is reasonable. The implied bulge parameters $r_c = 5''.9$, $\log (r_c/1 \text{ kpc}) = -0.29$ and $\mu_0 = 16.33$ V mag arcsec^{-2} are normal for $M_B = -21.9$: the parameter correlations in Kormendy (1987*b*) predict $\log r_c = -0.44$ and $\mu_0 = 16.35$ V mag arcsec^{-2}.

Figure 5 (*lower panel*) shows the major-axis profile after subtraction of the stretched minor-axis bulge fit. This time no outer cutoff is required. The best-fitting luminosity model like equation (1) but without the factor $C(r)$ has $r_0 = 2''.18$ and $r_\bullet = 0''.34$. This will be referred to as nuclear disk model "E" (for exponential).

The above estimates of the bulge and nuclear brightness distributions are used in the next section to remove the bulge contamination in the nuclear spectra, and in §§ IV and V for seeing and projection corrections.

d) Nuclear Kinematics: Correction for Bulge Contamination

The major-axis results discussed so far are not accurate measurements of either the bulge or the nucleus. In the central 10″ the spectra are composites of bulge and nuclear light. But the bulge is slowly rotating and hot, while the nucleus is rapidly rotating and cold. The Fourier quotient program "averages" the two populations, but weights the cold one more highly than its relative contribution to the light (Whitmore 1980;

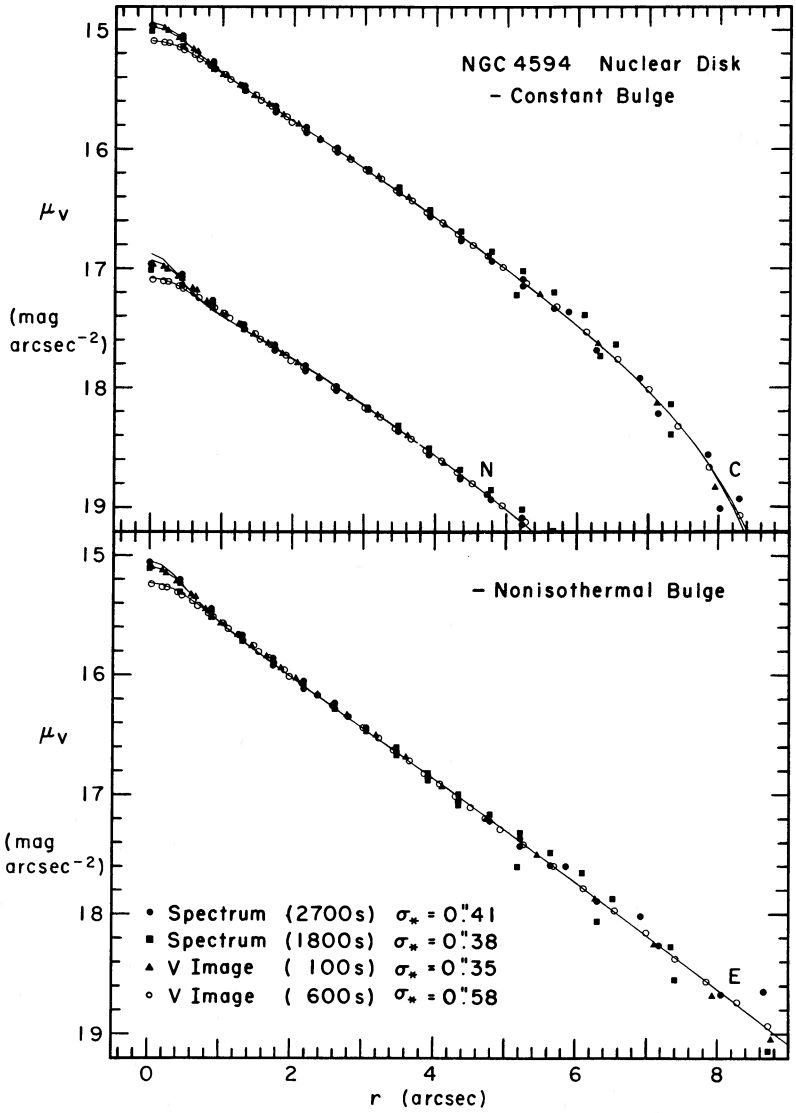

FIG. 5.—Major-axis brightness profile of NGC 4594 after subtraction of the bulge. In the upper panel, the surface brightness of the bulge is assumed to be 17.23 V mag arcsec^{-2}. The curves are nuclear disk luminosity model C convolved with seeing $\sigma_* = 0''.35$, $0''.40$, and $0''.58$. The same points and nucleus model N are also shown, shifted downward by 2 mag arcsec^{-2}. In the lower panel, the bulge brightness is assumed to be the nonisothermal profile fit (Fig. 4) scaled to the major axis. The lines are nucleus model E, similarly convolved with seeing.

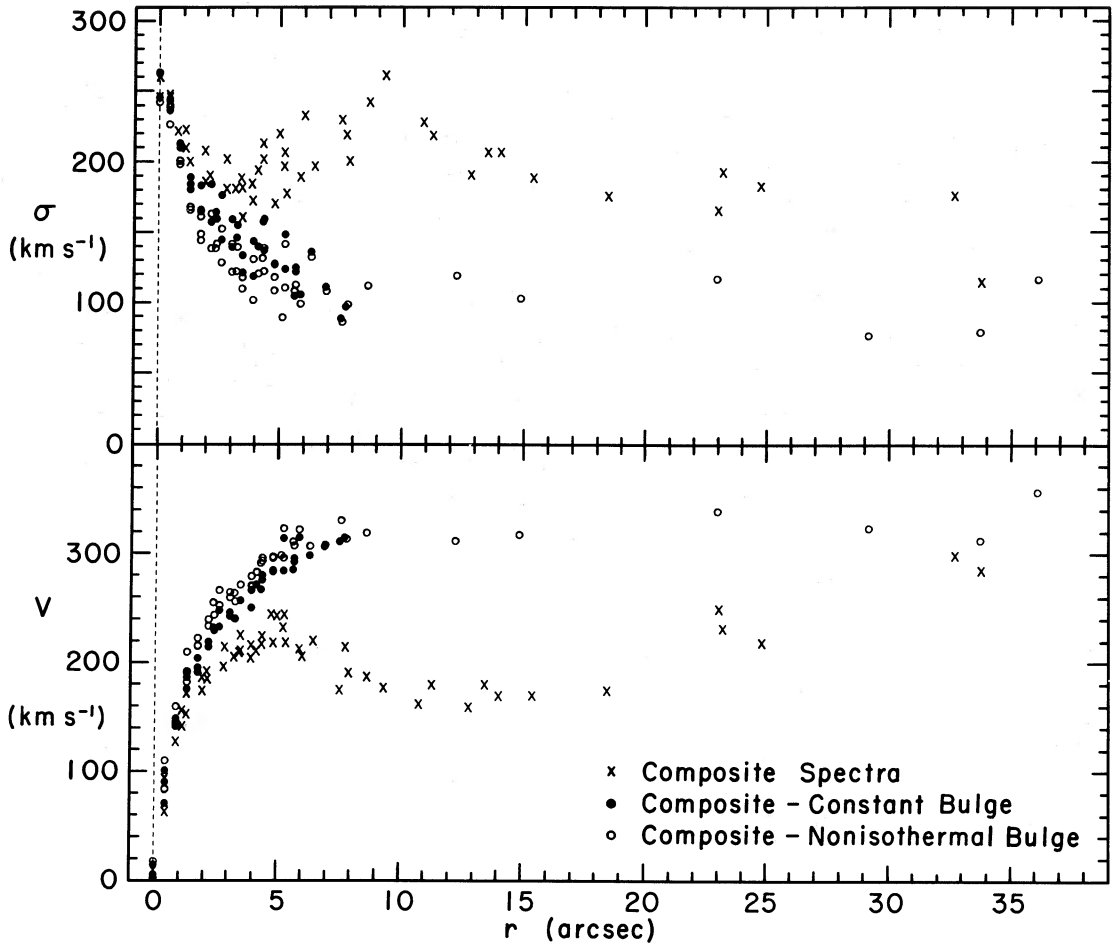

FIG. 6.—Rotation and dispersion curves along the major axis of NGC 4594 before and after subtraction of bulge light. Error bars are omitted for clarity but are shown in Figs. 1 and 9.

McElroy 1983). To measure the nucleus accurately, I need to subtract the bulge spectrum before running the Fourier program.

To do this, I first assume that the brightness of the bulge along the slit is 17.23 V mag arcsec^{-2}. For the bulge spectrum I use the mean of the minor-axis spectra at radii where the signal-to-noise ratio is large, i.e., at $r \leq 11''$ for the 2700 s exposure and $r \leq 6''.5$ for the 1800 s exposure. Bulge rotation is neglected (see below). The bulge spectrum is scaled to have a mean intensity of 1.0, multiplied into an image containing the brightnesses along the slit, and subtracted from the original spectra. The uncontaminated spectra of the nucleus are then analyzed with the Fourier program. The results are given in Table 2 and Figure 6.

As expected, the velocity gradients are larger than in Figure 1. The rotation curve rises to 310 ± 9 km s^{-1} at $r = 6''$–$8''$. The velocity dispersion of the nucleus falls rapidly from 255 ± 11 km s^{-1} at the center to 112 ± 11 km s^{-1} at $r = 6''$–$8''$ (cf. inner minimum $\sigma = 181 \pm 6$ km s^{-1} before bulge subtraction). The outer dispersion in the nucleus is similar to the mean $\sigma = 97 \pm 10$ km s^{-1} in the main disk. Both values are subject to systematic errors, e.g., due to imperfect bulge subtraction. However, it is clear that both disks are cold. Note that neither disk needs a large dispersion to ensure stability ($Q > 1$; Toomre 1964) because most of the gravity comes from the bulge.

The above results and those of subsequent sections do not depend strongly on details of the bulge subtraction. For example, I verified that bulge rotation does not make a significant difference, by subtracting a spectrum with the bulge rotation curve $V = (130$ km s$^{-1})$ $(r/80'')$ observed in KI. The resulting velocities and dispersions were almost always within 1 km s^{-1} of the tabulated values and rarely differed by more than 3 km s^{-1}.

As another test, I carried out a bulge subtraction based on the nonisothermal profile fit in Figure 4. The resulting rotation curve (Table 2; Fig. 6, *open circles*) is used in Kormendy and Westpfahl (1989) to determine the mass-to-light ratio of the bulge at $r \geq 8''$. The rotation curve rises to 318 ± 7 km s^{-1} at $r = 6''$–$9''$. It then stays flat or rises slowly over the inner part of the main disk. There is no longer a dip in the rotation curve at $r \sim 13''$; this was produced by the bulge. The velocities and dispersions are not very different from those given by the adopted decomposition. In particular, since V is larger and σ is smaller, and since both measure mass, the implied mass distribution is almost unchanged (§ V*e*).

IV. ANALYSIS TECHNIQUE

Section IV*a* discusses the methods used to derive volume velocity and velocity dispersion fields corrected for seeing. The derivation from these of masses and mass-to-light ratios $M/L_V(r)$ is discussed in § IV*b*. Calculation of the total luminosity $L_V(r)$ inside radius r also requires the total volume brightness distribution corrected for seeing; this is found in § IV*c*. Section V then uses this machinery to derive kinematic models and their corresponding mass distributions.

a) Seeing Modeling and Corrections

Volume velocity and velocity dispersion fields are derived as in Paper I and in Dressler and Richstone (1988). The calculation mimics the construction by seeing and projection of the observed spectra by adding up spectra of various V and σ from different parts of the galaxy. The spectra are weighted by the local volume brightness. This procedure is required because of the complicated response of the Fourier program to population mixes and to velocity smearing of spectra. Throughout the modeling, I assume that the nuclear disk is infinitely thin and edge-on; the calculation is then two-dimensional and short enough to allow a thorough exploration of parameter space.

The first step is to construct a library of input spectra. These are the spectrum of the standard star broadened to $\sigma = 100$–460 km s^{-1} in steps of 40 km s^{-1}; for each σ there are entries at $V = -1000$ to 1000 km s^{-1} in steps of 20 km s^{-1}. These values are confirmed with the Fourier program. I adopt trial volume luminosity, rotation, and dispersion distributions as discussed in § V. An output spectrum is calculated for each model pixel at radius r along the slit. Consider all other pixels at radius r' and depth z' along the line of sight. First I calculate the luminosity-weighted projected spectrum at r'. This pixel scatters light into the model pixel by an amount proportional to $I_*(r_*)$, where I_* is a star profile with the adopted σ_* and $r_* = r' - r$. Therefore the output spectrum is the sum over all scattering pixels of the projected spectra weighted by the product of the projected brightness and the star profile. The pixels used in the calculation are smaller by a factor of 5 than the real ones (1 pixel = 0.″087). The integration is carried out to a radius of 5 σ_* to include the non-Gaussian wings of the star profile. Finally, the model spectrum is analyzed with the Fourier program. The free parameters are then varied until the results fit the observed kinematics. The uncertainties are estimated by exploring the range of models allowed by the data, both in functional form and in the values of the free parameters.

b) Masses and Mass-to-Light Ratios

Given the run of I, V, and σ with radius, the mass inside r is calculated using the first velocity moment of the collisionless Boltzmann equation (cf. Sargent *et al.* 1978; Tonry 1987):

$$-\frac{d}{dr}(\rho\sigma^2) + \frac{\rho V^2}{r} = \frac{GM(r)\rho}{r^2}, \tag{3}$$

or

$$M(r) = \frac{V^2 r}{G} + \frac{\sigma^2 r}{G}\left(-\frac{d\ln\rho}{d\ln r} - \frac{d\ln\sigma^2}{d\ln r}\right). \tag{4}$$

Here G is the gravitational constant and ρ is the volume density of stars contributing to the spectra. I assume that M/L_V for these stars is independent of radius; then $d\ln\rho/d\ln r = d\ln I/d\ln r$. Equation (4) includes the approximations that the mean rotation is circular, that velocity distributions are isotropic, and that the mass distribution is spherical.

c) Total Volume Brightness Distribution

In the above, $I(r)$ is the unprojected brightness distribution of the stars that contribute to the spectra after bulge subtraction. However, $L_V(r)$ in M/L_V is the total light contained within radius r of the center, including the bulge. The derivation of $L_V(r)$ is intrinsically less certain than it was for M31. There seeing was not a problem, because the Stratoscope II photometry had very high resolution. Here I must explore carefully the range of central light concentrations allowed by the data.

The most convenient way to proceed is to find a sum of analytic functions that fits the observed profile after seeing convolution. I want to choose functions that have simple, preferably analytic deprojections. But the fits must be valid even at large radii, because these contribute to the projected brightness. This could be impossible, in which case a time-consuming numerical procedure would be required.

Fortunately, an $r^{1/4}$ law is an excellent fit over most of the projected mean profile (Fig. 7). A least-squares fit to the points at $r \geq 5''$ excluding the six discrepant values gives an effective radius $r_e = 102.''0$ and a central surface brightness of 13.022 V mag arcsec^{-2}. The corresponding total luminosity is $2.05 \times 10^{11}\ L_\odot$. The fraction of this contained inside radius r/r_e is tabulated in Young (1976).

It is now easy to fit the remaining light at the center with a function that has an analytic deprojection. A convenient function (Tonry 1987) is

$$\Sigma = \Sigma_0 \frac{1}{(1 + r^2/a^2)^{n-1/2}}, \tag{5}$$

where the central surface brightness Σ_0, the scale radius a, and the power $n - \frac{1}{2}$ are fitting parameters. The deprojection is

$$I(r) = I_0 \frac{1}{(1 + r^2/a^2)^n}, \tag{6}$$

where

$$\Sigma_0 = 2I_0\, an \int_0^\infty \frac{s^{1/2}}{(s+1)^{n+1}}\, ds\,. \tag{7}$$

The $r^{1/4}$ law already has a cuspy center, but it is easy to increase the central light concentration still further by increasing Σ_0 and decreasing a. Also, for most n of interest, $\Sigma(r)$ decreases rapidly enough at $r \gtrsim 5''$ that the outer fit is unaffected.

The best fit is shown in Figure 7. It has $\mu_0 = -2.5 \log \Sigma_0 = 15.37$ V mag arcsec^{-2}, $a = 1.''2$, and $n = 2.5$. It is conservative in that the volume brightness is too peaked at the center. However, this is due to the $r^{1/4}$ law: further increase of a does not help. I have chosen not to add the extra parameters that would be required to modify the $r^{1/4}$ law near the center to improve the fit.

The integrated luminosity corresponding to the above is

$$L(r) = 2\pi I_0 a^3 \int_0^{r^2/a^2} \frac{s^{1/2}}{(s+1)^n}\, ds\,. \tag{8}$$

The factor in front of the integral is $1.45 \times 10^9\ L_\odot$.

Best fits have also been found for smaller values of a. These are too centrally peaked to be acceptable, as are a pure power

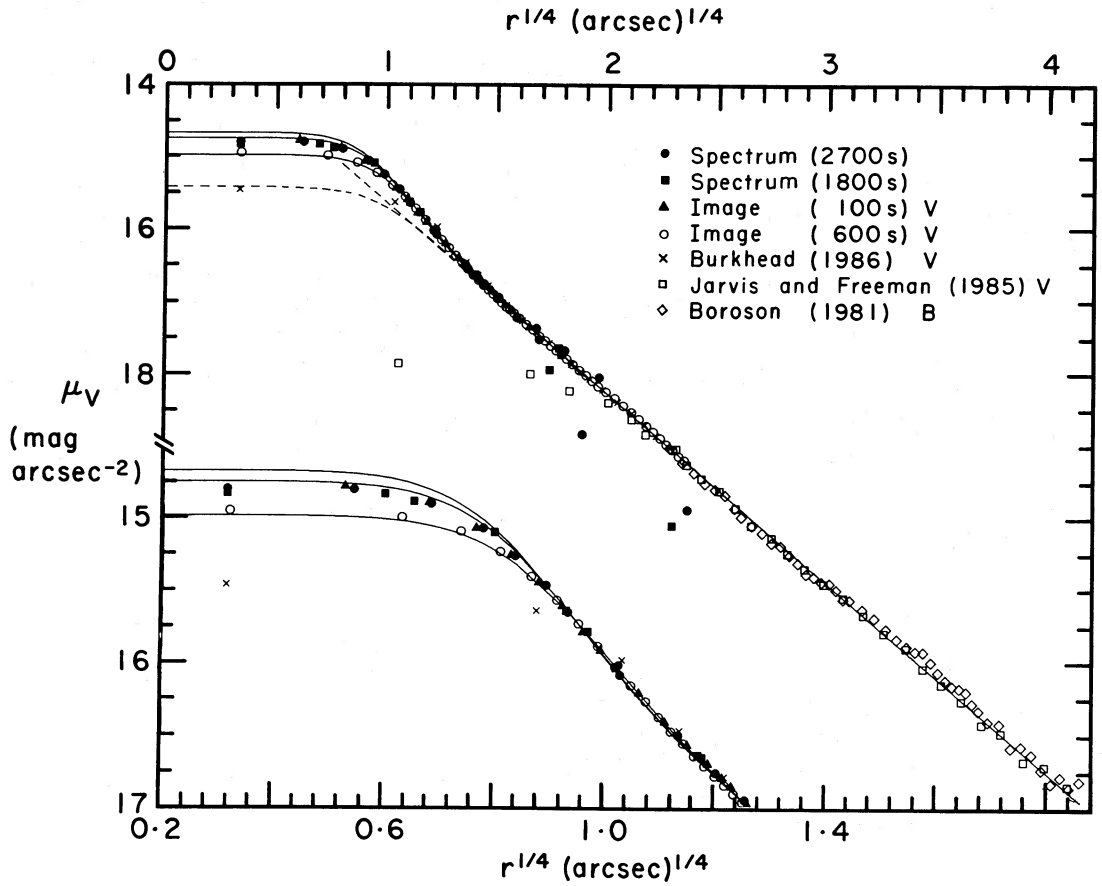

FIG. 7.—Projection of the total luminosity model $L_V(r)$ fitted to the mean profile of NGC 4594. The data points are minor-axis measurements scaled to the mean axis using the square root of the bulge axial ratio (Burkhead 1986, Fig. 9). The dashed lines are the $r^{1/4}$-law fit for seeing $\sigma_* = 0''.0$ and $\sigma_* = 0''.58$. The solid curves are the adopted total luminosity model, i.e., the above $r^{1/4}$ law plus eq. (5). The model has been convolved with seeing $\sigma_* = 0''.35$, $0''.40$, and $0''.58$. The scale is expanded at the bottom to better show the fit near the center.

law and a model that replaces the function (5) with a stellar nucleus.

The sum of the $r^{1/4}$ law and equation (5) reproduces the total magnitude observed inside radius r with very good accuracy. The most homogeneous data are photoelectric aperture measurements by van den Bergh (1976). For aperture radii of $2''.5$, $5''.0$, $7''.5$, and $10''.0$, the differences between the observed magnitudes V_{vdB} and the model magnitudes V are 0.005, 0.021, 0.007, and 0.010 mag. The mean is $\langle V_{vdB} - V \rangle = 0.011$ mag. There is no significant trend of the residuals with radius. That is, the correction for that part of the nuclear disk not included by the above luminosity model is negligible.

V. KINEMATIC MODELS: MASS DISTRIBUTIONS

The first two models discussed below are the best that I found. Model 1 has the virtue of being simple, and model 2 is the best fit to the data. Both imply that NGC 4594 contains a dark central mass of $M_\bullet \sim 10^9\ M_\odot$. In §§ Vc–Ve, I then vary the assumptions to see how $M_\bullet$ is affected. In particular, I look for a fit that does not imply a central mass concentration. Parameters of the models are given in Table 4. The intrinsic rotation and dispersion profiles are shown in Figure 8, the fits to the kinematic data in Figure 9, and the mass and mass-to-light ratio profiles in Figure 10.

a) Model 1

A remarkably simple model fits the data reasonably well. This has $V = 335$ km s^{-1} at all radii. The dispersion profile is the steepest possible, a "Keplerian" $\sigma(r) = \sigma_K r^{-1/2}$ km s^{-1}; $\sigma_K = 265$ km s^{-1} is the dispersion at $1''$. The best fit is obtained when σ is restricted to the range 100–400 km s^{-1}.

Figure 9 shows that model 1 provides an acceptable but not ideal fit. The rotation curve rises a little too slowly; it will be easy to remedy this by assuming a larger rotation velocity near the center. The dispersion profile also rises too slowly. This is caused by the sensitivity of the Fourier quotient to dispersions of ~ 100 km s^{-1}. It is easy to see why. Almost all wavenumber bins are affected by dispersions of 100 km s^{-1}, while few contain the contributions $\sigma \gtrsim 300$ km s^{-1}. The discrepancy in σ_0 is produced by a very small amount of low-σ light. The modeling procedure is designed to cope with such population mixes; it is reacting to the imperfect approximations. For example, the low σ_0 could be a result of the two-dimensional calculation. It could also be due to undersubtraction of the bulge, since this increases the luminosity weight of the cold disk in the calculation. The effect is important only in the central $1''$; as soon as the highest dispersion decreases a little, the weighting in the Fourier program becomes reasonable.

It is important to note that the observations are insensitive to dispersions larger than 400 km s^{-1}, whether real or pro-

TABLE 4

KINEMATIC MODELS

Model (1)	$I(r)$ (2)	V_c (km s^{-1}) (3)	V_K (km s^{-1}) (4)	V'_E (km s^{-1}) (5)	r'_0 (arcsec) (6)	V_E (km s^{-1}) (7)	r_0 (arcsec) (8)	σ_K (km s^{-1}) (9)	V_{max} (km s^{-1}) (10)	σ_{max}, σ_N (km s^{-1}) (11)	$M_\bullet^{0.1}$ ($10^9 M_\odot$) (12)	$M_\bullet$ ($10^9 M_\odot$) (13)	$\langle M/L_V \rangle$ (14)
1.....	C	335	...	...	...	...	...	265	...	400	0.7	3.2	3.4
2.....	C	...	380	...	...	305	3.3	265	500	300	0.8	4.0	3.0
3.....	C	...	...	470	0.2	300	3.5	265	...	400	0.6	4.2	2.9
4.....	C	...	...	305	0.6	290	3.7	265	...	400	0.5	3.2	3.3
5.....	C	...	...	260	1.0	285	4.1	265	...	400	0.4	2.4	3.4
6.....	N	335	...	...	...	...	...	265	...	400	0.2	2.6	3.6
7.....	N	...	410	...	...	300	3.7	270	1000	400	2.0	4.4	2.9
8.....	N	...	...	305	0.6	290	3.7	265	...	400	0.03	2.6	3.6
9.....	E	355	...	...	...	...	...	220	...	300	0.5	2.7	3.5
10.....	E	...	395	...	...	325	3.5	220	400	300	0.6	3.0	3.3
11.....	E	...	...	300	1.0	295	4.5	220	...	400	0.5	1.8	3.7

NOTES.—Col. (1): model number (Figs. 8–10). Col. (2): nuclear disk luminosity model (§ III*c*). Col. (3)–(8): rotation curve parameters. All models except 1, 6, and 9 consist of two components added in quadrature. Col. (3): constant velocity. Col. (4): Keplerian velocity at 1″. Cols. (5) and (6): maximum velocity and scale length of inner exponential-disk $V(r)$. Cols. (7) and (8): same for outer exponential $V(r)$. Col. (9): "Keplerian" velocity dispersion at 1″. Cols. (10) and (11): maximum total rotation velocity and velocity dispersion. For models 6–8, σ_N is the velocity dispersion of the unresolved nucleus. The minimum velocity dispersion is 100 km s^{-1} for all models. Col. (12): central mass estimated by the mass contained within 0″.1 of the center. Col. (13): central mass estimated by requiring that the mass-to-light ratio at $0''.7 \lesssim r \lesssim 8''$ (col. [14]) be as nearly constant as possible. The distance of NGC 4594 is assumed to be 18.0 Mpc.

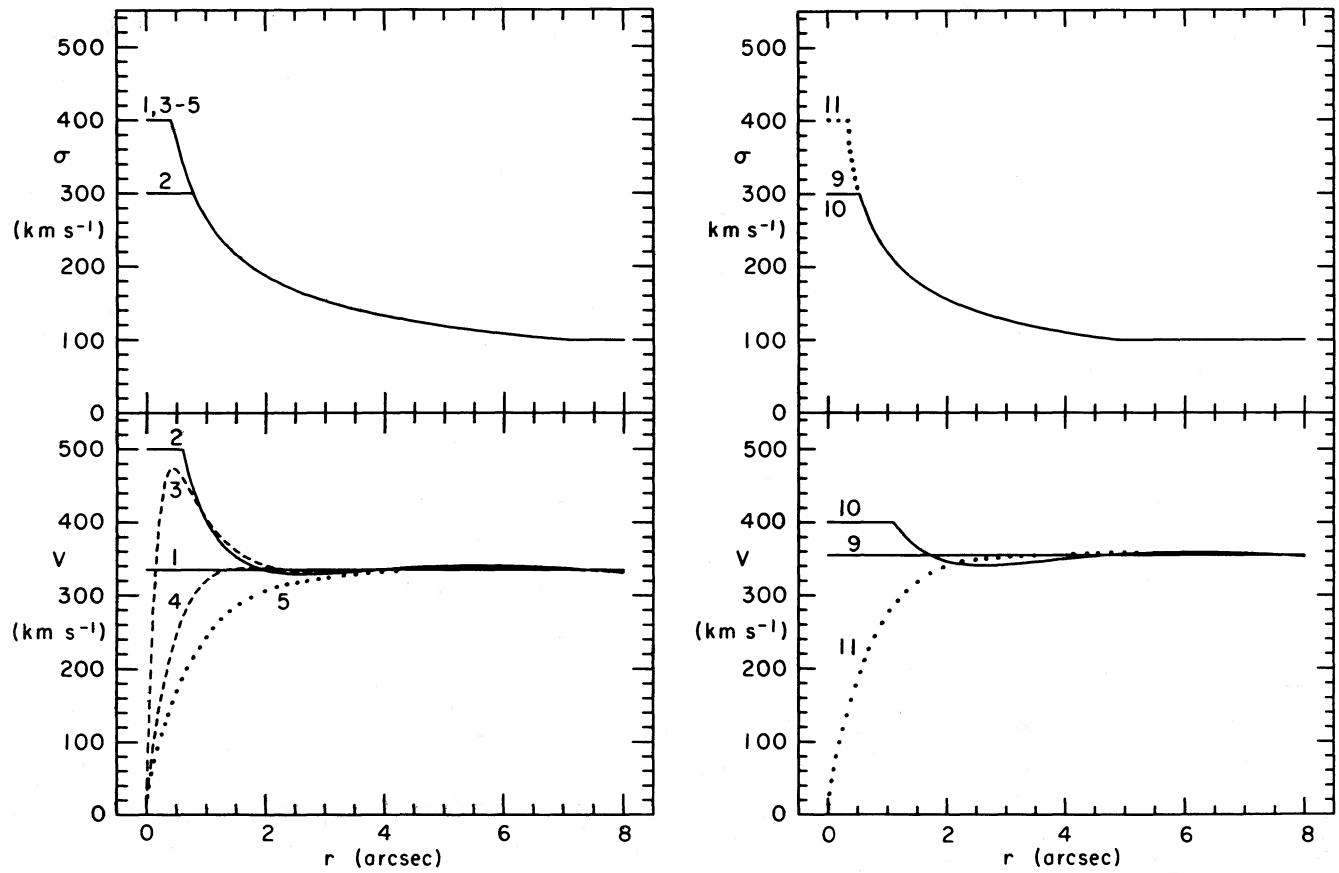

FIG. 8.—Intrinsic rotation and dispersion curves of the models fitted to the bulge-subtracted kinematic data. These are unprojected velocities not convolved with seeing. Model numbers are from Table 4.

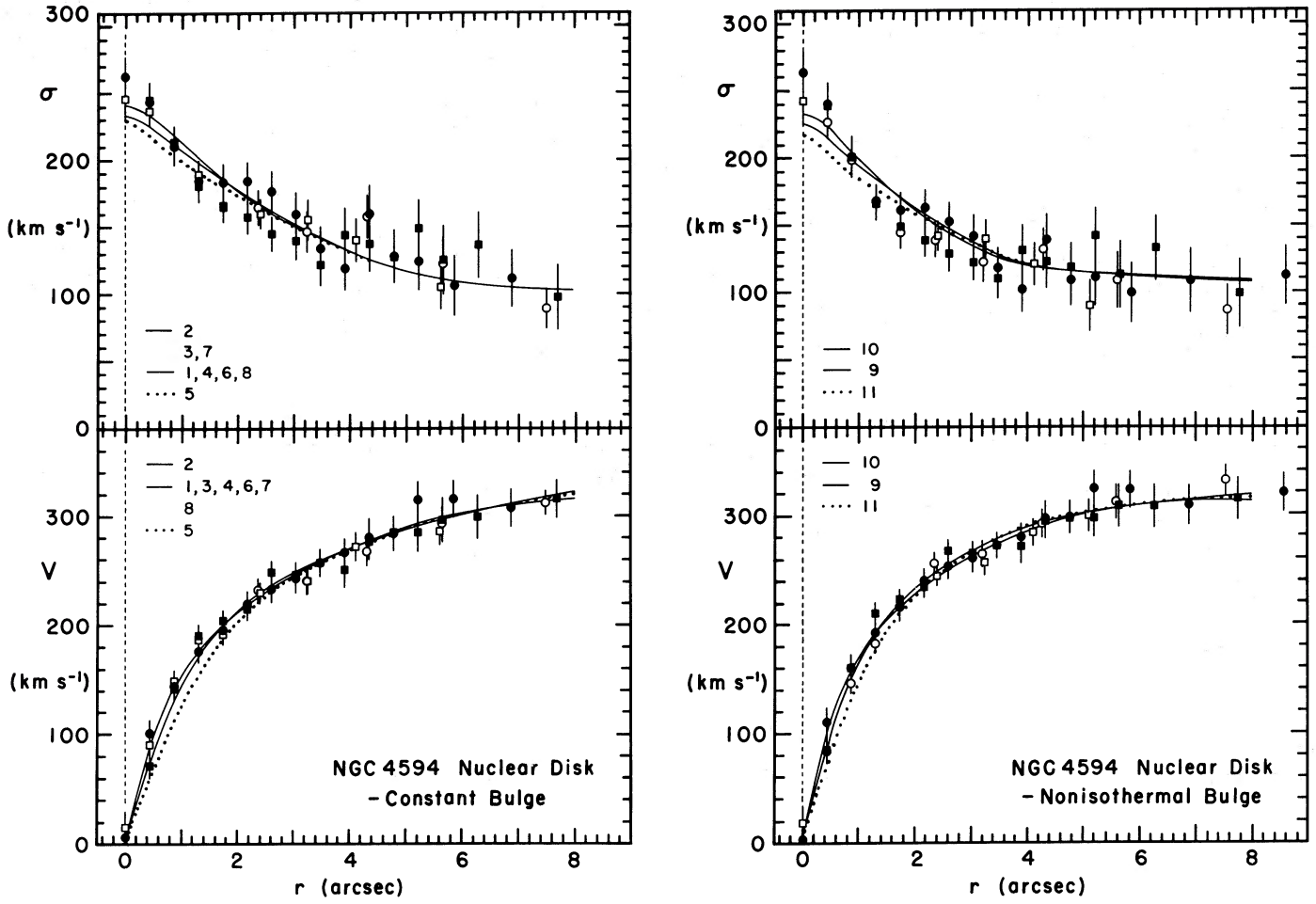

FIG. 9.—Model fits to the bulge-subtracted kinematic data. The lines show rotation velocities and velocity dispersions after projection and seeing convolution. Model numbers (Table 4) are given in the key in the same vertical order as the curves near the center. When a curve is labeled with more than one number, the first model is the one illustrated and the others are similar. Models with no associated curve in the key are not illustrated, but are intermediate between the ones immediately above and below.

duced by velocity smearing. These contribute to the Fourier quotient at wavenumbers outside the safe fitting range of the Gaussian. In physical terms, the corresponding line widths are too large compared with the wavelength interval observed and with the scale of continuum variations. This is a fundamental limitation of the instrumental setup, which was designed to allow measurement of dispersions of ~ 100 km s^{-1}. Given the small number of CCD pixels, I then cannot measure $\sigma \gg 400$ km s^{-1} if there is a contribution with $\sigma \simeq 100$ km s^{-1}. This situation will improve in future observing runs. Here I cannot give large weight to the fit to the central velocity dispersion.

Figure 10 shows that mass-to-light ratios derived from model 1 increase rapidly at $r < 1''$. At $r \gtrsim 3''$, $M/L_V \sim 4$ is the same in all of the models.

b) *Model 2*

The best fit to the data is given by a model like those constructed in Paper I for M31. The dispersion profile is the same as in model 1, except that the observed σ_0 is largest when the true σ is restricted to be ≤ 300 km s^{-1}. The rotation curve is the sum in quadrature of a Keplerian $V = V_K r^{-1/2}$ and the rotation curve of an exponential disk with maximum velocity V_E at $2.2r_0$ (Freeman 1970). The latter is only a convenient fitting function. It is necessary to limit the total rotation velocity to $V \leq 500$ km s^{-1}; much higher velocities result in lower σ_0 because the corresponding Fourier frequencies are outside the fitting range. This is model 2 in Figures 8–10. The fit to the rotation curve is essentially perfect; the fit to the dispersion profile is acceptable.

The mass distribution is slightly shallower than in model 1, and M/L_V rises a little more quickly toward the center. The difference is small because the larger rotation velocities in model 2 are partly offset by the smaller maximum σ. Both models imply that $M_\bullet \sim 10^9 M_\odot$.

c) *Models 3–5*

Is the detection of a central dark mass a robust result or only a consequence of the chosen forms of $V(r)$ and $\sigma(r)$? In the next three sections I try to model the data without such a mass. The fact that more complicated assumptions are required is in this context not a shortcoming.

First I replace the Keplerian $V(r)$ component with a second exponential. This allows me to decrease the amount of rotation near the center to zero. For example, model 3 is intermediate between models 1 and 2, except that $V \to 0$ at the center. The fit is not illustrated, but is also intermediate. The implied central

mass is larger because with less rotation at small r, a larger maximum velocity dispersion is required. But basically this model is like models 1 and 2.

To find the minimum M/L_V allowed, I need to know how large I can make the scale length r'_0 of the inner exponential. Model 4 has a more slowly rising rotation curve than any so far (Fig. 8); the projected, seeing-convolved $V(r)$ and $\sigma(r)$ are like those of model 1. Model 5 has a still larger $r'_0 = 1''.0$; now the predicted $V(r)$ definitely rises too slowly. If r'_0 is increased still further, the discrepancy grows rapidly. Not surprisingly, this model has the smallest central mass and M/L_V. Nevertheless, the data still imply that $M_\bullet \sim 10^9\ M_\odot$.

Interestingly, Figure 8 shows that the two exponentials in models 4 and 5 conspire to make rotation curves that rise quickly to ~ 335 km s^{-1} and then stay flat to $r > 8''$. Model 2 also has $V \simeq 335$ km s^{-1} at $r \gtrsim 2''$. It was this discovery that led to model 1.

d) Models 6–8: Stellar Nuclei

There is a degree of freedom here that I did not have in Paper I. I can postulate that NGC 4594 contains an unresolved nucleus. This can decrease $M_\bullet$, for two reasons. If the observed dispersion gradient is partly caused by a hot nucleus, it no longer contributes in equation (4). If the nucleus has unknown size, it can have almost arbitrarily high σ without telling us anything about $M_\bullet$. This is the situation in M87; it is the reason why Sargent *et al.* (1978) carefully interpreted only the core properties and not the nucleus. The same effect is not relevant in NGC 4594, because $\sigma(r)$ already reaches the adopted maximum value (Table 4) at several tenths of an arcsecond. However, adding a stellar nucleus also decreases $M_\bullet$ because $|d \ln I/d \ln r|$ for the distributed light is reduced in equation (4).

Models 6–8 are constructed using nuclear disk luminosity model N (§ IIIc). Recall that this puts too much light in the nucleus (Fig. 5). The resulting models are not acceptable fits to the data, but they clarify how securely a central mass is detected.

Models 6 and 7 (not illustrated) are like models 1 and 2, both in construction and in how well they fit the kinematic data. Model 6 implies a somewhat smaller value of $M_\bullet$ than model 1 (Table 4). But model 7 shows that larger central masses are also allowed. Because of the nucleus, the luminosity weighting of rotation is smaller near the center. As a result, higher Keplerian velocities are required, and an upper cutoff in V no longer improves the fit. Then M/L_V formally reaches 380 at $0''.1$ radius. Still higher mass-to-light ratios are possible.

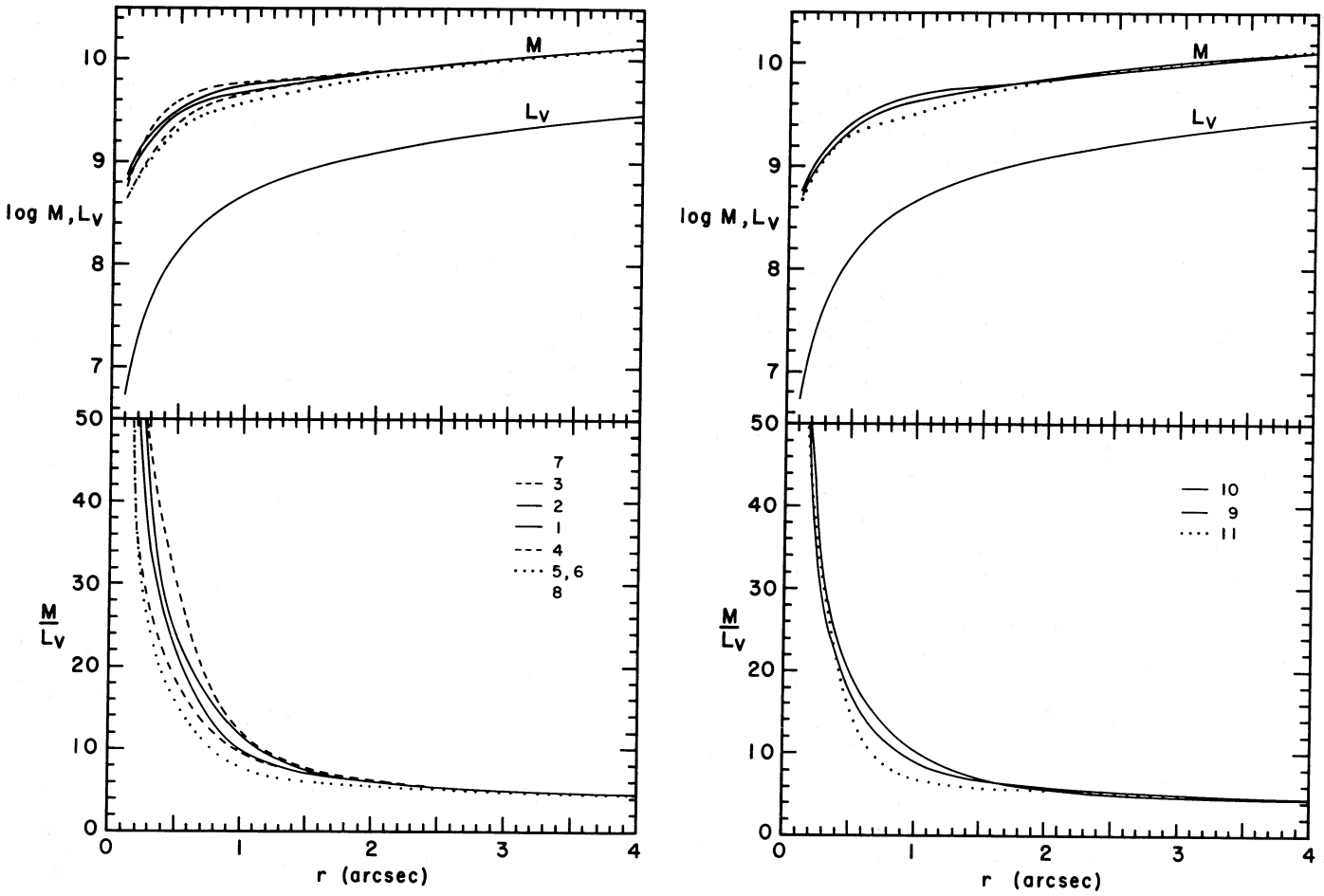

FIG. 10.—Integrated mass M, luminosity L_V and mass-to-light ratio M/L_V (solar units) interior to radius r as a function of r for the models in Figs. 8 and 9. The key is constructed as in Fig. 9. When V and σ reach limiting values (Table 4), there is a kink in the mass curves. A sudden limit is only an approximation to a gradual leveling off in velocity. I have not added extra parameters to model this, but have just interpolated through the $M(r)$ and $M/L_V(r)$ curves over the $0''.4$ centered on the kink.

At the same time, M/L_V can be substantially reduced. In model 8, I use the sum of two exponentials to approximate the shallowest plausible rotation curve. With a stellar nucleus present, the result is like model 4. Then M/L_V reaches a maximum of ~ 12 at $r \simeq 0''.5$ and then drops to 6 at the center. The best-determined part of this curve (at $r \geq 1''$) still implies that $M_\bullet \simeq 2.6 \times 10^9\ M_\odot$. Nevertheless, if model 8 were an acceptable fit to the data, the evidence for a central dark mass would not be compelling.

However, this model strains the error budget. (1) Nuclear disk luminosity model N is not an acceptable fit to the photometry. (2) The apparent rotation curve rises too slowly. Also, all of the models underestimate the central mass-to-light ratio, (3) because the dispersion profile rises too slowly toward the center and (4) because $L(r)$ is a little too peaked toward the center (§ IV*c*). I conclude that the central increase in M/L_V shown by models 1–5 is a robust result.

e) Models 9–11: Alternative Bulge Subtraction

Models 1–8 are based on the conservative bulge subtraction: the bulge was assumed to have constant brightness at $r \leq 10''$. In §§ III*c* and III*d*, I also derived the kinematics of the nuclear disk by assuming that the bulge is like the mean nonisothermal core of bright elliptical galaxies. Models 9–11 are fits to these data (Figs. 8–10).

Model 9 is like model 1: $V(r)$ is constant at all radii. The fit to the rotation curve is excellent. The fit to $\sigma(r)$ is slightly worse than before; the model predicts too small a dispersion gradient near the center. As noted earlier, rotation velocities are slightly larger and velocity dispersions at intermediate radii are slightly smaller with this bulge subtraction. Since both contribute comparably to $M(r)$, the changes in the implied mass and M/L_V profiles are small. The implied central mass concentration is only a little smaller than in model 1.

Model 10 is like model 2, the sum of a Keplerian and the rotation curve of an exponential disk. The Keplerian adds enough rotation at the center to make the kinematic fit as good as possible. Since little extra rotation is needed (Fig. 8), the use of a Keplerian is arbitrary. The fit to $\sigma(r)$ is improved as a by-product. This is the best model for the nonisothermal bulge subtraction; $M(r)$ and $M/L_V(r)$ are close to the mean for models 1–5.

Model 11 is analogous to model 5. The Keplerian is replaced by a second exponential $V(r)$ whose scale length $r_0' = 1''.0$ is made so large that the projected and seeing-convolved rotation curve rises too slowly. Rotation then adds little to the velocity dispersion near the center, so the predicted σ_0 is much too small. This model is again used to test the detection of a central mass. The derived mass is smaller than before but still clearly present. Therefore the attempt to explain the observations without a central dark object is unsuccessful.

f) Central Dark Mass

The value of the central dark mass is estimated in Table 4 in two ways. First, $M_\bullet^{0.1}$ is the total mass interior to $r = 0''.1$ (Fig. 10). The value of $M_\bullet^{0.1}$ is very sensitive to seeing corrections and to large velocities and dispersions poorly measured with the present instrument setup. Therefore an alternative, more reliable estimate $M_\bullet$ is derived. When $M_\bullet^{0.1}$ is subtracted from the $M(r)$ curves, a mass-to-light ratio gradient always remains; M/L_V rises by a factor of 4–15 in the central 5″. Requiring the residual M/L_V to be as nearly constant is possible gives a central mass of $M_\bullet$. The value of $M_\bullet$ is less sensitive to seeing or to instrumental problems; Table 4 shows that it is considerably more stable than $M_\bullet^{0.1}$. Differences between $M_\bullet$ and $M_\bullet^{0.1}$ values for different models provide one error estimate for the mass of the central dark object.

The mean mass-to-light ratio left when $M_\bullet$ is subtracted (Table 4, col. [14]) is near the lower envelope of values normally seen in cores of galaxies with $M_B \simeq -21.9$ (Kormendy 1987*a*, *b*). The mass-to-light ratio as a function of radius is discussed in Kormendy and Westpfahl (1989).

VI. DISCUSSION

This paper contains two main conclusions. First, at $r < 10''$ in NGC 4594 there is a well-defined nuclear disk of stars which is not obviously connected to the main disk at larger radii. Second, the mass-to-light ratio rises abruptly at $r < 1''$ to values $M/L_V \gtrsim 50$ at least 10 times as large as those at $r > 2''$. This implies the presence of a central dark mass $M_\bullet = 10^{8.5}$–$10^{9.5}\ M_\odot$.

Distinct nuclei like those in M31 and NGC 4594 are common in early-type disk galaxies (Kormendy 1985*a*). It is not known whether all of these are disks. However, NGC 3115, another edge-on galaxy with evidence for a central BH, also contains a nuclear disk (Kormendy and Richstone 1989). Such disks may be related to nuclear dust rings observed frequently in both bulges and ellipticals ($S0_3$ galaxies; Sandage 1961). These rings are seen especially often at the high resolution given by the CFHT (Kormendy and Stauffer 1987), because the dust tends to settle near the core radius, and core radii are small. They may also be related to the proposed process of powering nuclear activity by feeding central BHs. Could gas that is transported inward and fed to BHs form dust rings and stellar nuclei along the way when the density gets high enough in the gravitational funnel? In fact, could such nuclei play an important role in the formation of BHs in the first place? Central relaxation times in well-resolved cores of bright galaxies are too large to allow core collapse in a Hubble time. To make BHs, some other mechanism is required (Kormendy 1988*b*).

Central relaxation times can be interestingly short in nuclei as dense as those of M31 and NGC 4594. Figure 11 shows the relaxation time of the visible matter inside radius r as a function of r. I omit the central mass concentration and use the mean mass-to-light without the "BH" (Table 4) to derive $M_{vis}(r) \simeq 3.5L(r)$ from the luminosity model. The upper panel shows $M_{vis}(r)$. The lower panel shows the Spitzer and Hart (1971) half-mass relaxation time,

$$t_r = 0.060 \left(\frac{Nr^3}{Gm}\right)^{1/2} \frac{1}{\log\,(0.4N)}\,, \tag{9}$$

where $N(r) = 2M(r)/m$ is the number of stars corresponding to half-mass radius r. All stars are assumed to have the same mass m. The above is only a rough approximation. I have ignored the fact that the subsystem of radius r is not isolated. I have neglected rotation; its effects on relaxation are poorly understood. Probably most important is the fact that a central object of $10^9\ M_\odot$ will have compressed the visible mass distribution. Initial relaxation times were probably longer than I have shown. On the other hand, relaxation is faster if the nucleus is flattened. I conclude that core collapse near the center of the nucleus may have been possible. Certainly such a nucleus is a better prospect for forming a seed BH by relaxation processes than a normal galactic core. If this happened, the BH would

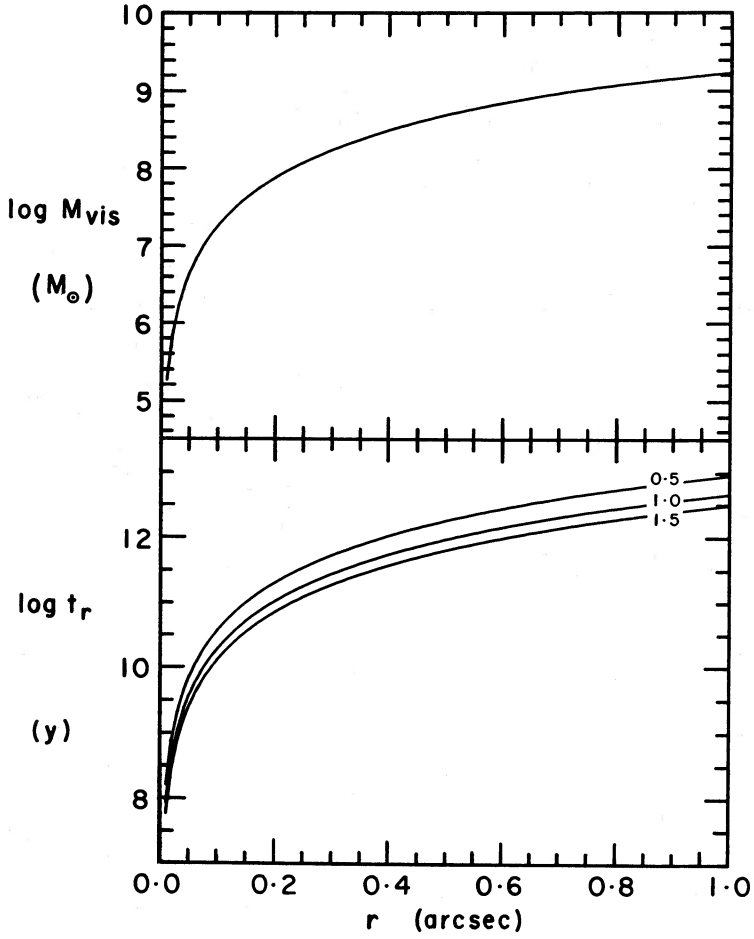

FIG. 11.—*Upper panel*: Integrated visible mass $M_{vis}(r) \simeq 3.5 L_V(r)$ inside radius r, where $L_V(r)$ is the luminosity model in Fig. 7. *Lower panel*: Half-mass relaxation time inside radius r for the above mass distribution assuming that all stars have the same mass $m = 0.5$, 1.0, or 1.5 $M_\odot$.

have been much smaller than $M_\bullet$ (Fig. 11). But it could easily have grown to $10^9\ M_\odot$ if it was the engine for a quasar or a powerful radio galaxy (Rees 1984).

Alternatively, the same dissipational process that made the nucleus may have transported enough material to the center to form a BH.

The interpretation of the central mass concentration is less certain than it was in M31. NGC 4594 is considerably more distant. The central mass is larger, but the increase in M/L_V takes place over a larger radius range ($\sim$90 pc). Also, the limited wavelength coverage makes the observations insensitive to dispersions $\sigma \gtrsim 400$ km s^{-1}. This is a problem near the center: the inferred velocity dispersion already reaches such values at several tenths of an arcsecond. Finally, a $10^9\ M_\odot$ cluster of 1.5 $M_\odot$ neutron stars could have survived without core collapse if its half-mass radius was $10^{-2.5}$ to $10^{-0.5}$ arcsec.

On the other hand, even more than in M31, Figure 10 and Kormendy and Westpfahl (1989) show that the mass-to-light ratio is remarkably constant over a large radius range and then suddenly increases near the center. A comparison of $M_\bullet \simeq 10^9\ M_\odot$ with the visible mass distribution (Fig. 11, *top*) emphasizes the difficulty of making such a large central mass out of remnants of ordinary stars. The central mass equals the visible mass in a sphere of radius $\sim 1''$, but even if the dark matter were distributed over this sphere, relaxation would not have concentrated it to the center as observed. The dark mass could be remnants only if the initial mass function of star formation was very strongly weighted toward massive stars in the central few tenths of an arcsec and nowhere else. Alternatively, nonbaryonic dark matter cannot be excluded as an explanation (cf. Rubin 1987). Thus the observations suggest but do not conclusively prove that the central mass concentration is a BH of mass $\sim 10^9\ M_\odot$.

The detection of BH candidates in M31 and M32 was ironic in that both galaxies are very inactive. NGC 4594 does show nuclear activity, although at a lower level than in radio galaxies and quasars. There is a compact nuclear radio source with a moderately high luminosity of $\sim 10^{39}$ ergs s^{-1} (e.g., van der Kruit 1973; de Bruyn *et al.* 1976; Graham, Weiler, and Wielebinski 1981; Preuss 1984). VLBI measurements by Shaffer and Marscher (1979) give a poorly determined size of $\lesssim 0''.0027 = 0.2$ pc. Lo (1986) has noted that the nuclear source in NGC 4594 is similar to that in our Galaxy but 10^5 times more powerful. The galaxy also shows optical activity: it contains a low-ionization nuclear emission-line region (LINER; Heckman 1980) or, more specifically, a dwarf Seyfert 1 nucleus (Filippenko and Sargent 1985, 1987). The full width at zero intensity of the Hα line is $\sim$5400 km s^{-1}. Filippenko and Sargent find that such activity is very common in nearby bright galaxies. The success rate of finding central mass concentra-

tions suggests that they, too, are common. The simplest interpretation is that we have begun to detect the gravitational signatures of supermassive black holes responsible for the wide range of nuclear activity in galaxies.

Note added in manuscript.—The Jarvis (1987) measurements have now been analyzed in Jarvis and Dubath (1988). They also find the kinematic features shown here in Figure 1. Jarvis and Dubath conclude independently that NGC 4594 contains a central mass of $\sim 10^9\ M_\odot$. I thank B. Jarvis for sending his preprint.

I thank C. Christian, P. Waddell, and the rest of the CFHT staff for their support of the observing run. I am especially grateful to D. Salmon for his care in setting up the f/4 module of the Herzberg spectrograph. It is a pleasure to thank J. Hutchings for obtaining a V image of NGC 4594 to help settle the question of whether there is a bright unresolved nucleus. M. Burkhead kindly provided his photometry in tabular form; helpful conversations with him, with A. Filippenko, and with S. D. Tremaine are gratefully acknowledged.

REFERENCES

Bahcall, J. N., and Wolf, R. A. 1976, *Ap. J.*, **209**, 214.
Boroson, T. 1981, *Ap. J. Suppl.*, **46**, 177.
Brault, J. W., and White, O. R. 1971, *Astr. Ap.*, **13**, 169.
Burkhead, M. S. 1986, *A.J.*, **91**, 777.
de Bruyn, A. G., Crane, P. C., Price, R. M., and Carlson, J. B. 1976, *Astr. Ap.*, **46**, 243.
Dressler, A. 1984, *Ap. J.*, **286**, 97.
Dressler, A., and Richstone, D. O. 1988, *Ap. J.*, **324**, 701.
Filippenko, A. V., and Sargent, W. L. W. 1985, *Ap. J. Suppl.*, **57**, 503.
———. 1987, in *IAU Symposium 121, Observational Evidence of Activity in Galaxies*, ed. E. Ye. Khachikian, K. J. Fricke, and J. Melnick (Dordrecht: Reidel), p. 451.
Freeman, K. C. 1970, *Ap. J.*, **160**, 811.
Graham, D. A., Weiler, K. W., and Wielebinski, R. 1981, *Astr. Ap.*, **97**, 388.
Heckman, T. M. 1980, *Astr. Ap.*, **87**, 152.
Jarvis, B. 1987, *ESO Messenger*, No. 49, p. 15.
Jarvis, B. J., and Dubath, P. 1988, *Astr. Ap.*, in press.
Jarvis, B. J., and Freeman, K. C. 1985, *Ap. J.*, **295**, 324.
Kormendy, J. 1985*a*, *Ap. J. (Letters)*, **292**, L9.
———. 1985*b*, *Ap. J.*, **295**, 73.
———. 1987*a*, in *IAU Symposium 127, Structure and Dynamics of Elliptical Galaxies*, ed. T. de Zeeuw (Dordrecht: Reidel), p. 17.
———. 1987*b*, in *Nearly Normal Galaxies: From the Planck Time to the Present*, ed. S. M. Faber (New York: Springer-Verlag), p. 163.
———. 1988*a*, in *Supermassive Black Holes*, ed. M. Kafatos (Cambridge: Cambridge University Press), p. 98.
———. 1988*b*, in *Supermassive Black Holes*, ed. M. Kafatos (Cambridge: Cambridge University Press), p. 219.
———. 1988*c*, *Ap. J.*, **325**, 128 (Paper I).
Kormendy, J., and Illingworth, G. 1982, *Ap. J.*, **256**, 460 (KI).
Kormendy, J., and Richstone, D. O. 1989, in preparation.
Kormendy, J., and Stauffer, J. 1987, in *IAU Symposium 127, Structure and Dynamics of Elliptical Galaxies*, ed. T. de Zeeuw (Dordrecht: Reidel), p. 405.
Kormendy, J., and Westpfahl, D. J. 1989, *Ap. J.*, **338**, in press.
Lauer, T. R. 1985, *Ap. J.*, **292**, 104.
Lo, K. Y. 1986, *Science* **233**, 1394.
Lo, K. Y., Backer, D. C., Ekers, R. D., Kellermann, K. I., Reid, M., and Moran, J. M. 1985, *Nature*, **315**, 124.
McElroy, D. B. 1983, *Ap. J.*, **270**, 485.
Morgan, W. W., and Keenan, P. C. 1973, *Ann. Rev. Astr. Ap.*, **11**, 29.
Preuss, E. 1984, in *IAU Symposium 110, VLBI and Compact Radio Sources*, ed. R. Fanti, K. Kellermann, and G. Setti (Dordrecht: Reidel), p. 251.
Rees, M. J. 1984, *Ann. Rev. Astr. Ap.*, **22**, 471.
Richstone, D. O. 1987, in *IAU Symposium 127, Structure and Dynamics of Elliptical Galaxies*, ed. T. de Zeeuw (Dordrecht: Reidel), p. 261.
———. 1988, in *Supermassive Black Holes*, ed. M. Kafatos (Cambridge: Cambridge University Press), p. 87.
Rubin, V. C. 1987, in *IAU Symposium 117, Dark Matter in the Universe*, ed. J. Kormendy and G. R. Knapp (Dordrecht: Reidel), p. 51.
Rubin, V. C., Burstein, D., Ford, W. K., and Thonnard, N. 1985, *Ap. J.*, **289**, 81.
Salmon, D. 1985, *CFHT Information Bull.*, No. 13, 9.
Sandage, A. 1961, *The Hubble Atlas of Galaxies* (Washington: Carnegie Institution of Washington).
Sargent, W. L. W., Schechter, P. L., Boksenberg, A., and Shortridge, K. 1977, *Ap. J.*, **212**, 326.
Sargent, W. L. W., Young, P. J., Boksenberg, A., Shortridge, K., Lynds, C. R., and Hartwick, F. D. A. 1978, *Ap. J.*, **221**, 731.
Schechter, P. L., and Gunn, J. E. 1979, *Ap. J.*, **229**, 472.
Shaffer, D. B., and Marscher, A. P. 1979, *Ap. J. (Letters)*, **233**, L105.
Spitzer, L., and Hart, M. H. 1971, *Ap. J.*, **164**, 399.
Tody, D., *et al.* 1986, *IRAF User Handbook* (Tucson: NOAO).
Tonry, J. L. 1984, *Ap. J. (Letters)*, **283**, L27.
———. 1987, *Ap. J.*, **322**, 632.
Toomre, A. 1964, *Ap. J.*, **139**, 1217.
van den Bergh, S. 1976, *A.J.*, **81**, 797.
van der Kruit, P. C. 1973, *Astr. Ap.*, **29**, 249.
Walker, G. A. H., Johnson, R., Christian, C. A., Waddell, P., and Kormendy, J. 1984, in *State-of-the-Art Imaging Arrays and Their Applications*, ed. K. N. Prettyjohns (*Proc SPIE*, Vol. **501**), p. 353.
Whitmore, B. C. 1980, *Ap. J.*, **242**, 53.
Whitmore, B. C., McElroy, D. B., and Tonry, J. L. 1985, *Ap. J. Suppl.*, **59**, 1.
Young, P. J. 1976, *A.J.*, **81**, 807.

JOHN KORMENDY: Dominion Astrophysical Observatory, Herzberg Institute of Astrophysics, 5071 West Saanich Road, Victoria, BC V8X 4M6, Canada